

Explainable Deep Neural Network for Multimodal ECG Signals: Intermediate vs Late Fusion

Timothy Oladunni¹, Ehimen Aneni²

¹Computer Science Department, Morgan State University and Yale University

Timothy.oladunni@morgan.edu; timothy.oladunni@yale.edu

²Section of Cardiovascular Medicine, Department of Internal Medicine, Yale University

School of Medicine

ehimen.aneni@yale.edu

ABSTRACT The limitations of unimodal deep learning models, particularly their tendency to overfit and limited generalizability, have renewed interest in multimodal fusion strategies. Multimodal deep neural network (MDNN) has the capability of integrating diverse data domains and offers a promising solution for robust and accurate predictions. However, the optimal fusion strategy, intermediate fusion (feature-level) versus late fusion (decision-level), remains insufficiently examined, especially in high-stakes clinical contexts such as ECG-based cardiovascular disease (CVD) classification. This study investigates the comparative effectiveness of intermediate and late fusion strategies using ECG signals across three domains: time, frequency, and time-frequency. A series of experiments were conducted to identify the most performing fusion architecture. Results demonstrate that intermediate fusion consistently outperformed late fusion, achieving a peak accuracy of 97%, with Cohen's $d > 0.8$ relative to standalone models and $d = 0.40$ compared to late fusion. Interpretability analyses using saliency maps reveal that both models align with the discretized ECG signals. Statistical dependency between the discretized ECG signals and corresponding saliency maps for each class was confirmed using Mutual Information (MI). The proposed ECG domain-based multimodal model offers superior predictive capability and enhanced explainability, a crucial attribute in medical AI applications, surpassing state-of-the-art models.

INDEX TERMS Multimodal, deep learning, neural networks, cardiovascular diseases, CVD,

1. INTRODUCTION

Most neural network models in ECG signal processing rely on unimodal inputs [1], typically derived from limited features such as time-domain signals alone [2, 3, 4]. Some studies relied only on frequency domain features [5, 6, 7]. Other works were done using only time-frequency domain features [8, 9, 10]. Although these approaches yield some predictive success, they overlook the complementarity and synergistic information present across multiple domains. As a result, they fail to fully exploit the rich diagnostic potential of ECG signals, which encode clinically relevant patterns in diverse domains (time, frequency, and time-frequency).

The unimodal modeling strategy may introduce algorithmic bias and limit generalizability in real-world clinical settings [11], where models disproportionately overfit a group of

patient populations or clinical conditions. Such bias undermines diagnostic reliability and contributes to healthcare disparities [12], impeding the equitable deployment of AI in cardiology. Addressing this challenge requires a more holistic and domain-informed modeling strategy that accounts for the complementarity and synergies of information in diverse domains.

Multimodal deep neural networks continue to gain prominence in AI for biomedical applications, and their ability to integrate heterogeneous data sources is becoming central to advancing predictive accuracy and clinical robustness. However, the opacity of these models is a significant challenge. This study aims to develop and evaluate an AI-driven ECG explainable diagnostic framework that enhances CVD detection and mitigates algorithmic bias through complementary domain fusion.

Building upon earlier work [13], which has leveraged mutual information to investigate redundancy and complementarity within multimodal ECG datasets for optimized model performance, the present study introduces a novel application: utilizing mutual information as a quantitative metric for validating the fidelity and informativeness of Explainable AI (XAI) methods applied to complex multimodal ECG models. This approach addresses a critical gap in the field, moving beyond mere visual interpretability to provide a rigorous, data-driven assessment of XAI explanations in a crucial clinical context.

A multimodal deep learning model that fuses feature representations extracted from time-domain, frequency-domain, and time-frequency domain analyses of ECG signals, with a quantifiable explainability, is hereby proposed. The proposed model is designed to capture necessary and sufficient features from the complete PQRST complex [14], thereby enhancing its capability to detect cardiovascular disease (CVD) with higher fidelity, reliability, and accuracy.

Goal of Study

The overarching goal of this study is to improve the reliability, interpretability, and fairness of ECG-based CVD diagnostics by designing a multimodal fusion architecture that unifies the synergistic strengths of the time, frequency, and time-frequency domains of the ECG signal. This approach is empirically validated to enhance clinical reliability and align with trustworthy AI principles in healthcare.

Contribution

This study will make significant contributions to multiple domains:

- 1. Comprehensive Multimodal Model Benchmarking & Optimal Strategy Identification:** Eight novel multimodal and three unimodal deep learning models are designed, developed, and systematically evaluated for ECG-based cardiovascular disease classification. The intermediate fusion model (M4) outperformed all.
- 2. Enhanced Robustness and Generalizability:** The robustness and generalizability of the proposed methodology were rigorously assessed using a suite of statistical and diagnostic evaluations. Performance consistency was quantified using Cohen's d effect sizes, and 95% confidence intervals for $\Delta F1$ were estimated via bootstrap resampling.
- 3. Improved Interpretability Fidelity Assessment:** Saliency maps were aligned with raw ECG waveform. Assessment was based on divergence,

sparsity, and attention variance. Established sanity checks for saliency maps, including randomizing model weights and shuffling training labels, were also performed, confirming that the saliency maps robustly reflected genuinely learned patterns rather than spurious input artifacts.

- 4. Resilience to Noise:** Controlled ablation studies were done under noise conditions (e.g., Gaussian noise, baseline wander), demonstrating that the intermediate fusion model (M4) retained strong performance, further supporting its potential applicability in real-world clinical environments.
- 5. Advancing Quantifiable, Explainable, and Ethical AI in Healthcare:** This study introduces a novel, quantifiable framework for Explainable Artificial Intelligence (XAI) in multimodal ECG analysis. Mutual Information (MI) was integrated as an objective measure of saliency relevance. It offers measurable insight into model decision-making.
- 6. Synthetic Data Physiological Plausibility Assessment:** The physiological plausibility methods include feature space analysis, visual inspection, evaluation of deep feature consistency, and Kullback-Leibler (KL) Divergence. This ensures data integrity and supports the development of fair, interpretable, and ethically aligned models, promoting equity and accessibility in AI-driven healthcare.
- 7. Clinical Translation:** The experimental findings reveal that domain-based ECG multimodal models achieve high accuracy and impressive interpretability, while providing an enlightening perspective on the transformative potential of multimodal deep learning in cardiovascular disease diagnosis.

We provide a fresh, comprehensive view of the applications of artificial intelligence (AI) in healthcare. The proposed model emphasizes the potential of multimodal deep learning to support real-time, interpretable, and highly accurate cardiovascular diagnostics. It also offers a valuable tool for future clinical implementation and holds promise for wider applications in multimodal disease diagnosis.

This paper is organized as follows: Section 1 discusses the introduction to the study. The methodology of the experiment is discussed in Section 2. Section 3 highlights the experiment. The discussion and conclusion of the study are presented in Sections 4 and 5, respectively.

2. METHODOLOGY

2.1. Overview

This study systematically investigates both unimodal and multimodal deep learning approaches for the classification of cardiovascular diseases (CVDs) using electrocardiogram (ECG) signals represented across three complementary domains: time, frequency, and time-frequency. The dataset used consists of four distinct classes: Normal, Myocardial Infarction (STEMI), History of STEMI, and Abnormal Heartbeat. To ensure high-quality signal input, the raw ECG recordings underwent a comprehensive preprocessing pipeline that included wavelet-based denoising and Butterworth bandpass filtering to remove baseline wander, high-frequency noise, and irrelevant spectral components. Following preprocessing, class imbalance [15] was addressed using the Adaptive Synthetic Sampling (ADASYN) technique [16], enabling more robust learning across all disease classes.

Each domain-specific representation was mapped to an architecture optimized for its structure and information characteristics. The time-domain signals were processed using a one-dimensional convolutional neural network (1D-CNN) designed to capture local temporal features and morphological patterns. For the time-frequency domain, continuous wavelet transform (CWT) was applied to convert ECG signals into spectrogram-like images, which were then analyzed using a two-dimensional convolutional neural network (2D-CNN) to extract spatial and temporal-spectral correlations. The frequency-domain signals, derived via Fast Fourier Transform (FFT), were input into a Transformer-based architecture to capture long-range dependencies and global frequency patterns.

To leverage the complementarity of these modalities, fusion strategies were implemented at the early, intermediate (feature-level), and late (decision-level) stages. Early fusion combines domain-specific features at the input level, allowing the classifier to exploit cross-domain interactions from the outset. Intermediate fusion involved the concatenation of deep features extracted from each unimodal pathway before classification, while late fusion utilized a weighted ensemble of individual model predictions.

Model training employed the Adam optimizer with categorical cross-entropy loss. Training convergence was regulated using early stopping based on validation performance. The models were evaluated using multiple classification metrics, including accuracy, precision, recall, and F1-score, to ensure comprehensive performance assessment. Finally, model

explainability using gradient-based saliency mapping [16] was performed post hoc. These visualizations highlighted the regions of the input signals that had the most significant influence on the model's output, thereby offering insights into domain-specific discriminative features.

2.2. Deep ECG Multimodal Fusion Pipeline

Figure 1 presents a generic ECG signal processing and multimodal fusion pipeline adopted in this study. The workflow begins with the acquisition and preprocessing of raw ECG signals, including denoising and bandpass filtering to enhance signal quality and suppress noise artifacts. The preprocessed signal is then decomposed into three distinct analytical domains of Time, Frequency, and Time-Frequency. Each domain captures complementary characteristics of the cardiac cycle. These domain-specific representations serve as inputs to deep learning models, which are integrated using one of three fusion strategies: early fusion (at input level), intermediate fusion (at feature level), or late fusion (at decision level). To enhance interpretability and clinical transparency, Explainable AI (XAI) techniques such as saliency maps are employed to visualize the model's decision rationale. Finally, comparative performance evaluation is conducted across all fusion configurations to determine the most effective and clinically meaningful approach.

2.3. Dataset

The dataset used for this study was obtained from Mendeley Data [17].

Summary of ECG Image Categories:

- **Myocardial Infarction (STEMI):**
240 patients \times 12 images = 2,880 images
→ Exhibits ST-segment elevation and T-wave abnormalities.
- **Abnormal Heartbeat:**
233 patients \times 12 images = 2,796 images
→ Shows irregular heart rhythms like arrhythmias.
- **History of STEMI:**
172 patients \times 12 images = 2,064 images
→ Features altered QRS complexes and delayed conduction from past STEMI events.
- **Normal Individuals:**
284 patients \times 12 images = 3,408 images
→ Displays well-defined PQRST waveforms with minimal variations.

ECG Signal Processing and Fusion Pipeline

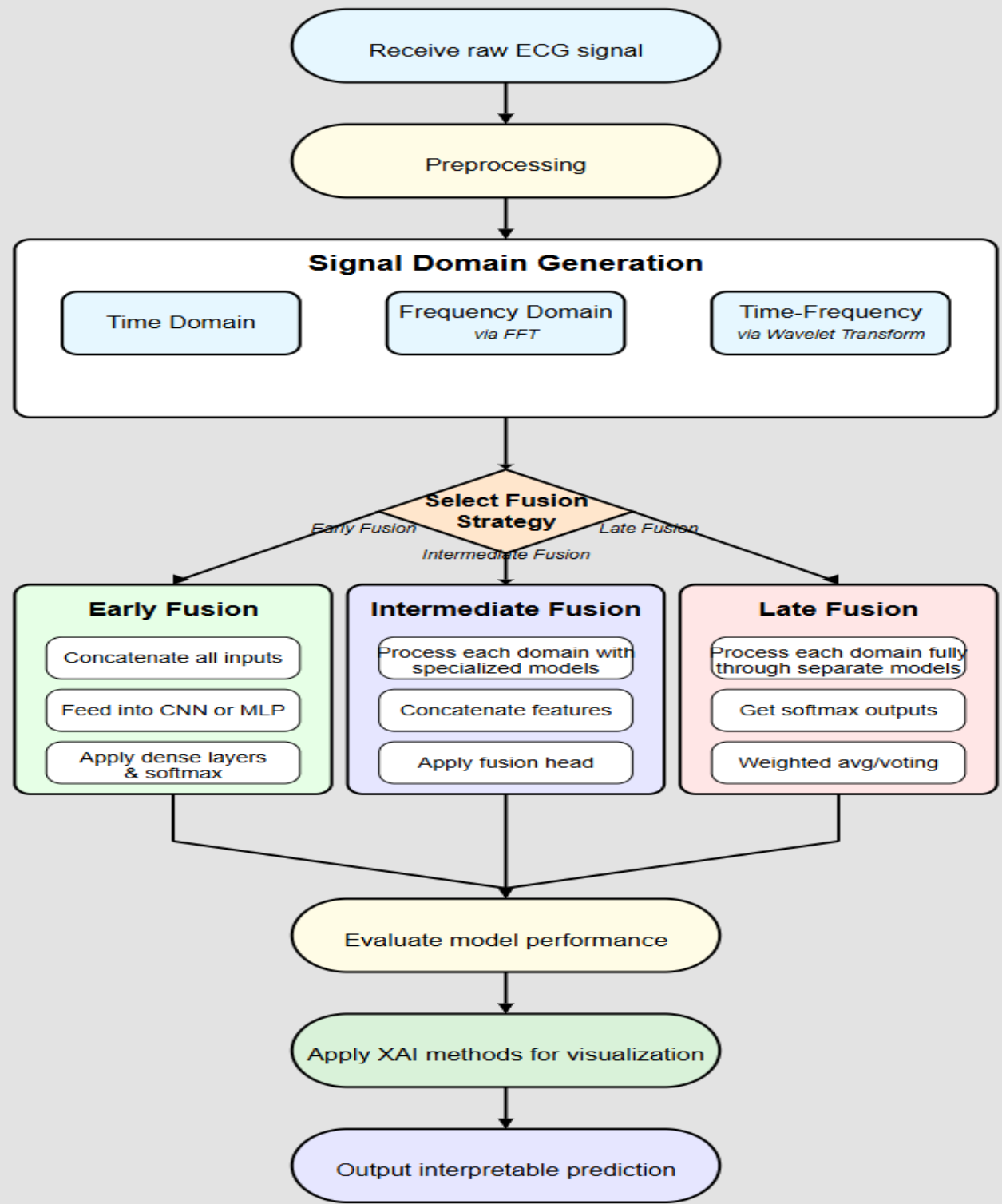


Figure 1. ECG Signal Processing and Fusion Pipeline. Raw ECG signals are preprocessed to remove noise and filter signals outside a specified range. Pre-processed signals are decomposed into time, frequency and time-frequency domains. Early, intermediate and late fusion strategies are employed for multimodalities. Final outputs are evaluated for explainability and interpretability

2.1. Handling Class Imbalance with Adaptive Synthetic Sampling (ADASYN)

Addressing class imbalance is crucial for building effective classification models, especially with medical datasets. In these datasets, minority classes often hold significant clinical importance. For instance, the ECG dataset in this study exhibited a clear imbalance, with the History of Myocardial Infarction class being significantly smaller than the other classes. To tackle this, the **Adaptive Synthetic (ADASYN) sampling approach** [18] was deployed to balance the training set. Choosing the correct algorithm to balance medical data is crucial due to its sensitive nature; an incorrect choice could have severe consequences.

ADASYN was selected over other oversampling techniques, such as traditional Synthetic Minority Over-sampling Technique (SMOTE) [19], due to its adaptive nature, which is particularly well-suited for the inherent complexities of ECG data. Unlike SMOTE, which generates synthetic samples uniformly along the line segments connecting minority class instances and their nearest neighbors, ADASYN focuses on generating more synthetic samples for minority class examples that are "harder" to learn [20]. It achieves this by adaptively shifting the decision boundary and generating more synthetic data points for samples located closer to the majority class or in sparse regions of the feature space. The sensitivity of medical datasets makes the adaptive density-based generation of ADASYN a suitable choice for this purpose.

ADASYN offers several advantages for ECG classification:

1. **Addressing Complex Decision Boundaries:** ECG signals, even when represented by extracted features, often involve nonlinear and intricate decision boundaries that separate different physiological states. By concentrating synthetic sample generation in difficult-to-learn regions, ADASYN enables learning algorithms to develop more refined and robust decision boundaries that can better distinguish between subtle variations in ECG patterns.
2. **Mitigating Overlap and Ambiguity:** In medical data, there can be inherent overlap or ambiguity between classes, especially for rare conditions that share features with more common states. ADASYN's focus on samples near the decision boundary helps clarify these ambiguous regions by reinforcing the presence of the minority class where it is most needed, rather than uniformly oversampling easily distinguishable instances.
3. **Enhancing Feature Space Coverage:** For minority classes that might be sparsely distributed in the feature space, ADASYN effectively "fills in" these gaps more intelligently than uniform oversampling. This leads to a more comprehensive representation of the minority class's manifold,

enabling the model to generalize better to unseen, but physiologically plausible, variations.

By dynamically generating synthetic samples based on the local density of minority class examples, ADASYN aims not just to balance the class distribution but also to improve the overall learning performance by focusing on regions that are challenging for the classifier, making it a highly suitable choice for the ECG dataset.

Ultimately, ADASYN extends SMOTE by adapting the number of synthetic samples per instance based on the hardness of learning (i.e., local class imbalance) [21]. The idea is to focus more on ambiguous regions, improving the decision boundary. ADASYN was implemented using the following steps.

A. Define local class imbalance around a minority sample x_i :

$$r_i = \frac{\Delta_i}{k} \quad (1)$$

Where:

- Δ_i is the number of k nearest neighbors of x_i that belong to the majority class
- $r_i \in [0,1]$ quantifies how "difficult" or "ambiguous" that point is

B. Normalize difficulty weights:

$$G_i = \frac{r_i}{\sum_{j=1}^n r_j} \cdot G \quad (2)$$

Where:

- G is the total number of synthetic samples to generate
- G_i is the number of synthetic samples to generate for point x_i

This results in a more effective representation of underrepresented morphologies.

The mathematical formulation above is operationalized in Algorithm 1, which outlines the pseudocode for addressing class imbalance in the extracted time-frequency ECG representations. Specifically, Adaptive Synthetic Sampling (ADASYN) is applied after generating 2D wavelet scalograms, targeting regions where minority class samples are sparse or surrounded by majority class instances, which are 'hard' to learn. ADASYN adaptively generates synthetic examples in these regions to improve class balance and enhance model learning.

Algorithm 1: ADASYN Balancing of Time-Frequency ECG Features

I. Inputs:

$\mathcal{D} = \{(I_i, y_i)\}$: Set of ECG scalogram images and class labels
 $I_i \in \mathbb{R}^N(H \times W)$: 2D ECG time-frequency image
 $y_i \in \{1, 2, \dots, C\}$: Class label

II. Outputs:

$X_{\text{bal}} \in \mathbb{R}^{N' \times s \times s}$: Balanced scalogram matrix
 $Y_{\text{bal}} \in \{0,1\}^{N' \times C}$: One-hot encoded labels

III. Parameters:

L : Total number of minority samples to generate
 s : Desired image size after resizing (output resolution)
 k : Number of nearest neighbors (default: 5)

IV. Step 1: Image-to-Signal Conversion

For each image I_i :
 $x_i(t) = (1/W) \cdot \sum_{w=1}^W I_i(t, w)$ // Converts image row to 1D ECG signal by averaging columns

V. Step 2: Time-Frequency Representation

For each signal $x_i(t)$:
 $S_i(a, b) = \int x_i(t) \cdot \psi^*(a, b) (t) dt$ // CWT transform
 $S_i(a, b) = |S_i(a, b)|^2$ // Power scalogram
 $\tilde{S}_i = \text{Resize}(S_i, (s, s))$ // Resize to fixed shape

VI. Step 3: Feature Matrix Construction

$X = \{\tilde{S}_i\}$, $Y = \{y_i\}$ for $i = 1$ to N
 $x_i = \text{vec}(\tilde{S}_i) \in \mathbb{R}^{s^2}$ // Flatten scalogram

VII. Step 4: ADASYN Oversampling

For each minority class sample x_i :
Compute d_i : Degree of difficulty using k -NN
 $G_i = (d_i / \sum_j d_j) \cdot G$ // Adaptive weight
For each synthetic sample:
Choose neighbor x_j from k nearest
 $\lambda \sim \text{Uniform}(0, 1)$
 $x_{\text{new}} = x_i + \lambda(x_j - x_i)$ // Generate new point

VIII. Step 5: Reconstruction and One-Hot Encoding

Reshape $x_{\text{new}} \in \mathbb{R}^{s^2}$ to image format
Convert $y_i \in \{1, \dots, C\}$ → one-hot $\in \{0,1\}^C$
Return X_{bal} , Y_{bal}

2.2. Validation of Synthetic Sample Physiological Plausibility

Research question: How can the physiological plausibility of the synthetic dataset generated by the ADASYN be quantitatively and qualitatively evaluated to ensure its suitability for downstream ECG modeling tasks?

To address this question, a multifaceted validation approach was employed to rigorously assess the quality of the ADASYN-generated synthetic scalograms. This approach included feature space analysis, visual inspection, evaluation of deep feature consistency, and Kullback-Leibler (KL) Divergence.

2.2.1. Feature Space Distribution Analysis

The global distribution of both real and ADASYN-generated synthetic scalograms was assessed using t-distributed Stochastic Neighbor Embedding (t-SNE) [22, 23]. As shown in Figure 2, the synthetic samples consistently cluster within the high-density regions occupied by real samples across all four classes (Class 0–3). This spatial proximity in the reduced feature space indicates that the synthetic data preserves key statistical and structural properties of authentic ECG signals.

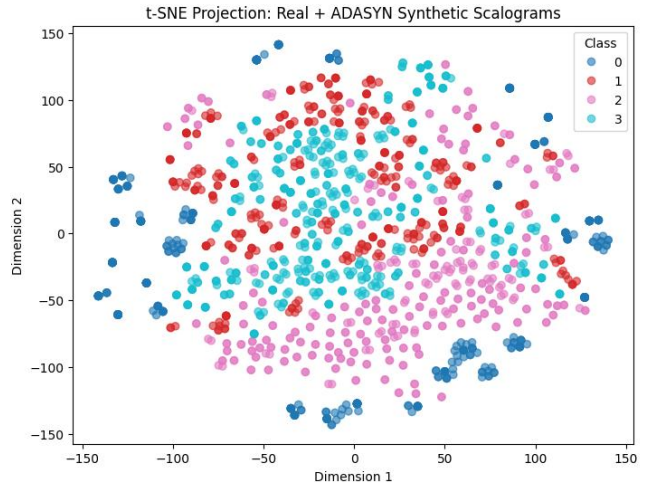
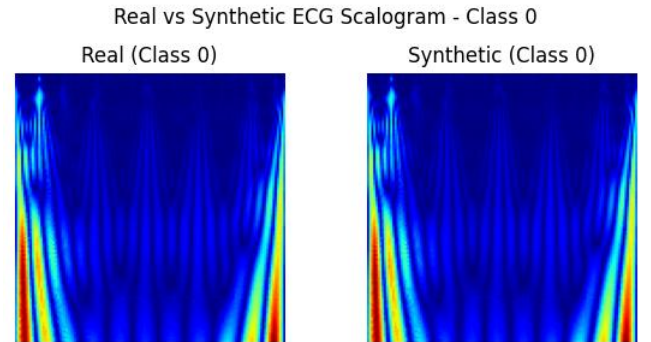


Figure 2. Global Distribution of both Real and ADASYN-generated synthetic scalograms

2.2.2. Visual Fidelity to Physiological Patterns

To qualitatively assess signal realism, synthetic scalograms were visually compared to real ones [24]. Figure 3 shows side-by-side examples illustrating that synthetic samples replicate time-frequency characteristics, energy distributions, and structural patterns commonly observed in ECG signals. The resemblance supports the hypothesis that the ADASYN-generated scalograms retain physiologically meaningful characteristics, while formal clinical validation remains outside the current scope.



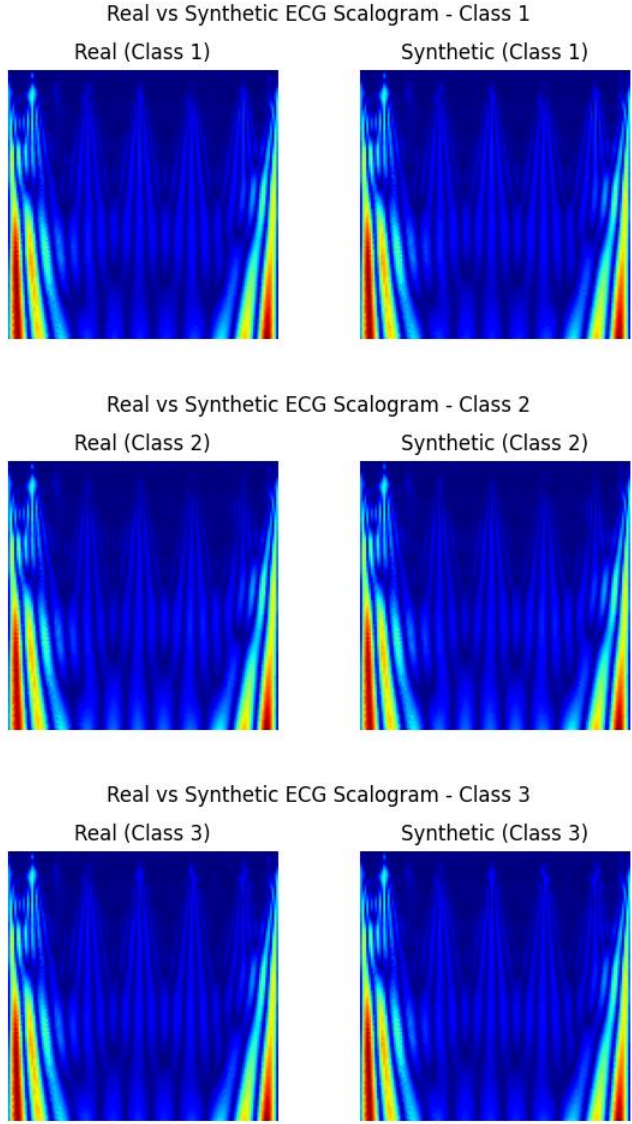


Figure 3. Visual comparison of real vs. synthetic ECG scalograms: morphology and energy distribution.

2.2.3. Consistency in Deep Feature Representation

To evaluate how a trained model interprets synthetic signals, feature representations were extracted from the `max_pooling2d_3` layer of the 2D-CNN. Intra-class cosine similarity was computed between real and synthetic samples, [25], with three examples per class. As visualized in Figure 4, real and synthetic samples elicited consistent deep activation patterns within each class. This substantial similarity in CNN-derived representations confirms that the synthetic data is encoded by the model in a manner consistent with real ECG inputs, supporting its utility for downstream training and generalization.

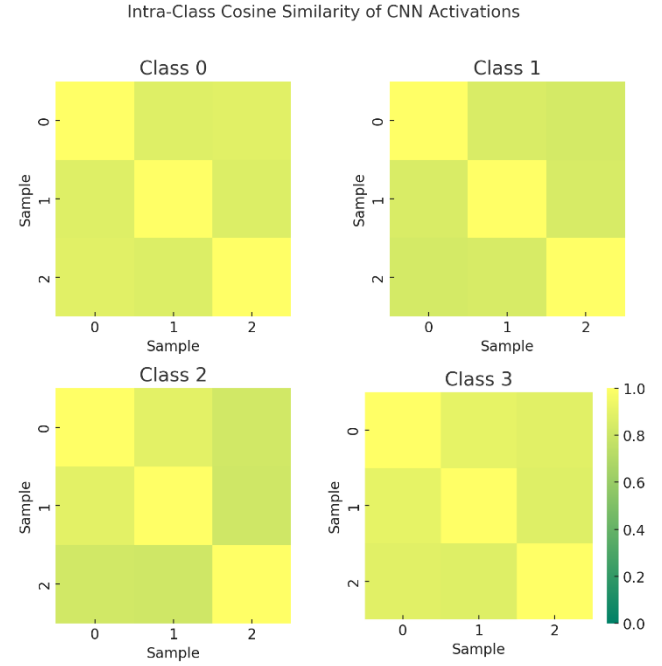


Figure 4. Cosine Similarity Heatmap

2.2.4. KL Divergence

Finally, a statistical analysis using Kullback-Leibler (KL) Divergence was computed. A remarkably low KL Divergence of 0.0008 was observed. As KL Divergence quantifies the divergence of one probability distribution from another, a value nearing zero strongly indicates that the synthetic data's distribution is nearly identical to that of the real data [26, 27].

The converging qualitative and quantitative empirical evidence from the above complementary evaluations conclusively demonstrates that the generated synthetic dataset is physiologically plausible and highly suitable for downstream ECG modeling tasks.

2.3. Wavelet Decomposition

Wavelet decomposition is a signal processing technique that decomposes a signal into different frequency components and provides multi-resolution analysis [28]. This is necessary for analyzing non-stationary signals, such as ECG, where the frequency of content changes over time. The decomposition results in two types of coefficients: approximation coefficients, which represent the low-frequency components of the signal, and detail coefficients, which represent the high-frequency components.

Equation 3 represents the decomposition of signal S into its approximation (A) and detail (D) coefficients at different levels (j). This process helps isolate important signal features and filter out noise.

$$S = A_j + \sum_{j=1}^J D_j \quad (3)$$

Where:

- A is the low-frequency approximation
- D are the high-frequency detail coefficients at level j .

2.3.1. Thresholding for Noise Removal

Signals are decomposed to compute the detailed coefficients D_j using soft thresholding.

$$D'_j = \text{sign}(D_j) \cdot \max(|D_j| - \lambda, 0) \quad (4)$$

Where λ is the noise threshold.

As shown in equation 4, the choice of the threshold λ is crucial. Coefficients with an absolute value smaller than λ are set to zero, effectively removing noise. Coefficients with an absolute value greater than λ are shrunk, preserving the signal while reducing noise. Thus, the choice of λ is critical; a small λ may leave too much noise, while a large λ may remove important signal features [29].

2.3.2. Signal Reconstruction

After the detail coefficients have been thresholded, the inverse wavelet transform is applied to obtain the filtered time-domain signal [30]. Equation (5) shows the inverse wavelet transform, where the approximation coefficients at the final level and the modified detail coefficients are used to reconstruct the signal. This step effectively converts the processed wavelet representation back into a meaningful ECG signal, with the noise components significantly reduced.

$$S' = A_j + \sum_{i=1}^j D'_i \quad (5)$$

2.3.3. Bandpass Filtering

Noises associated with the ECG dataset [31] was reduced using a Butterworth bandpass filter [32]. The Butterworth bandpass filter filtered out frequencies not within a specified range. Equation (6) represents the general bandpass filtering process.

$$H_{bandpass}(f) = H_{highpass}(f) - H_{lowpass}(f) \quad (6)$$

The selected frequency range should encompass the dominant frequencies of the P-wave, QRS complex, and T-wave [33].

2.3.4. Ablation Study

Research Question: What is the optimal frequency range that balances effective noise suppression while preserving critical diagnostic information for deep learning-based ECG classification in this application?

The above question was addressed through a rigorous ablation study. Using a 1D Convolutional Neural Network (1D-CNN) on ECG signals preprocessed with various bandpass filter configurations, three specific bandpass filter settings were

systematically evaluated. The goal was to pinpoint the range that maximizes classification accuracy and clinical utility.

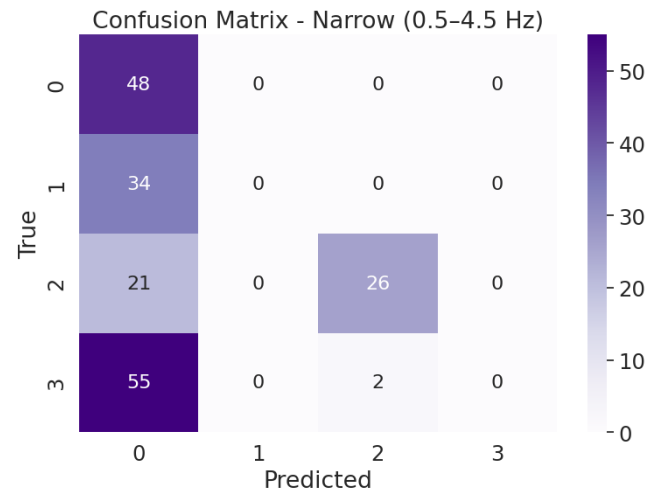
A 1D-CNN architecture was chosen specifically for this analysis because of its proven ability to directly capture localized temporal features like QRS complexes, P-waves, and T-waves from raw or minimally processed ECG time-series data [34]. This architecture's efficiency, low computational complexity, and strong baseline performance were crucial for its selection, as they enabled controlled experiments where the sole impact of preprocessing steps could be isolated, free from architectural variability [35].

The three bandpass filtering configurations include:

- I. A narrow 0.5–4.5 Hz filter focused on aggressive noise suppression (targeting baseline wander and high-frequency noise).
- II. A standard 0.5–45 Hz filter commonly adopted in ECG signal processing for diagnostic tasks.
- III. A wide 0.05–100 Hz filter enabling full-band signal admission, capturing both low-frequency drift and high-frequency detail.

The trained 1D-CNN model was evaluated across all three conditions. Confusion matrices and class-specific performance metrics revealed how filtering choices affect the model's ability to preserve clinically relevant information versus removing noise.

Figure 5 presents the corresponding confusion matrices for each configuration (ordered top to bottom: 0.5–4.5 Hz, 0.5–45 Hz, 0.05–100 Hz), providing empirical insight into the optimal trade-off between signal fidelity and denoising in ECG-based classification tasks.



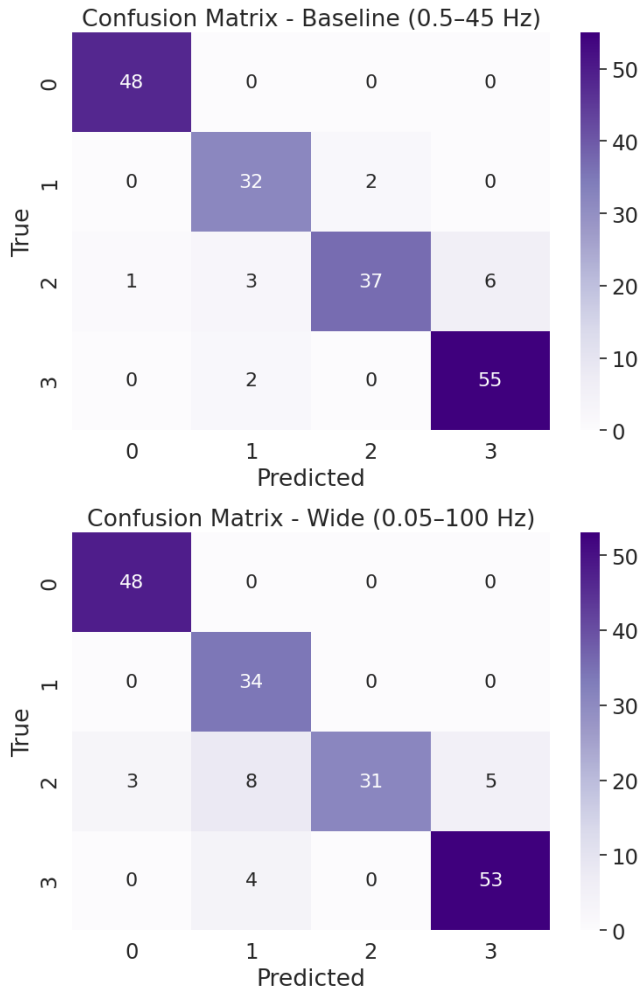


Figure 5. Confusion matrices comparing ECG classification performance under three bandpass filter settings: (Top) Narrow filter (0.5–4.5 Hz), (Middle) Baseline filter (0.5–45 Hz), and (Bottom) Wide filter (0.05–100 Hz).

- The narrow filter (0.5–4.5 Hz) severely distorts class boundaries, causing all minority classes to be misclassified predominantly as Class 0, reflecting over-suppression of physiologically relevant features.
- In the baseline configuration (0.5–45 Hz), class-wise predictions are highly accurate across all categories, with minimal confusion and balanced diagonal structure, particularly for Myocardial Infarction and Abnormal Heartbeat classes.
- The wide filter (0.05–100 Hz), while preserving all frequency content, introduces noise-induced confusion, especially between Class 2, likely due to baseline wander and Electromyogram (EMG) interference.

- These results empirically validate the 0.5–45 Hz filter as the best trade-off frequency between noise attenuation and waveform fidelity.

As shown in Figure 5, the baseline 0.5–45 Hz filter yields the best class separation, preserving the integrity of QRS, ST-segment, and T-wave. The narrow 0.5–4.5 Hz filter aggressively removes high-frequency noise but at the cost of physiological fidelity, resulting in high class confusion. Conversely, the wide filter allows excessively low- and high-frequency artifacts to enter the signal, degrading model performance through class boundary distortion. Table 1 summarizes the interpretation of the experimental results.

Table 1. Class-wise interpretation of filter performance and diagnostic trade-offs from the Confusion Matrix

Class	Narrow (0.5–4.5 Hz)	Baseline (0.5–45 Hz)	Wide (0.05–100 Hz)	Comment
Class 0	Accurate; QRS/ST-T well preserved	Accurate; QRS/ST-T well preserved	Accurate; QRS/ST-T well preserved	All filters provide clean separation and preserve morphology.
Class 1	Misclassified as Class 0; HRV features suppressed	Reduced precision	Correctly classified; RR and P variability retained	The narrow filter misclassified all.
Class 2	Heavily misclassified; ST/QRS slopes lost	High sensitivity; ST deviations moderately retained	Reduced precision	ST elevation features are lost in the narrow filter; baseline performs best.
Class 3	All misclassified; morphology overly flattened	Consistently detected; voltage-based features preserved	Slightly degraded; minor distortion of voltage features	Wide and narrow filters degrade voltage-sensitive patterns; baseline stable.

Performance evaluation based on Accuracy, Precision, Recall, and F1-Score is shown in Table 2. The baseline filter (0.5–45 Hz) demonstrated the best overall performance, striking a balance between noise suppression and signal preservation. The narrow band (0.5–4.5 Hz) led to substantial degradation

across all metrics, likely due to excessive attenuation of clinically relevant ECG components (e.g., QRS complex and T wave). The wide range (0.05–100 Hz) preserved more information but admitted higher-frequency noise, slightly reducing generalization performance.

Table 2. Performance Comparison Table

Filter Range	Accuracy	Precision	Recall	F1
Narrow (0.5Hz-4.5 Hz)	0.40	0.31	0.40	0.30
Baseline (0.5Hz-45 Hz)	0.92	0.93	0.92	0.92
Wide (0.05-100 Hz)	0.89	0.91	0.89	0.89

The results of the ablation study suggest a 0.5–45 Hz bandpass frequency as a pragmatic trade-off between artifact suppression and signal integrity, aligning with previous biomedical signal processing standards [36].

2.4. Data Splitting Strategy

A stratified splitting strategy was employed using the `StratifiedShuffleSplit` function from the `Scikit-learn` library to split the data into training, testing, and validation sets. The dataset was first partitioned into an 80% training set and a 20% test set using stratified sampling to preserve the original class distribution. Subsequently, the 20% test set was further split evenly into two subsets, resulting in a 10% validation set and a 10% held-out test set. The stratification approach ensures that all subsets retain the same proportional distribution of class labels as the original dataset.

2.5. Signal Processing

Figure 6 illustrates the PQRST complex of an electrocardiogram (ECG) signal, representing the sequence of electrical events that occur during a single heartbeat [37]. This waveform is divided into distinct segments: the P wave, PR interval, QRS complex, ST segment, and T wave. Each corresponds to specific phases of cardiac depolarization and repolarization [38]. In this study, signal processing techniques based on time, frequency, and time-frequency domains are applied, extracting feature representations from physiologically meaningful segments to support accurate classification of cardiovascular disease (CVD).

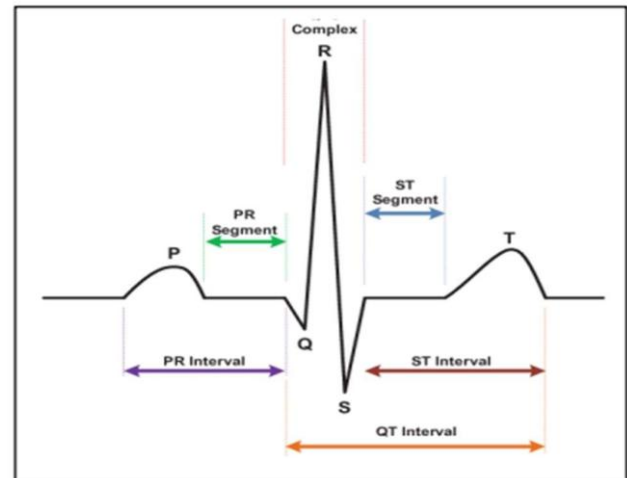


Figure 6. The PQRST Complex [39]. The diagram depicts the P wave, QRS complex and T wave. It also shows the PR and ST intervals with PR and ST segments. The ST segment and T wave correspond to the repolarization of the ventricles. The QT interval spans the total duration of ventricular depolarization and repolarization.

2.5.1. Time Domain

The PQRST complex of the ECG signal was algorithmically decomposed in the time domain to investigate the morphological characteristics of each segment. The P wave was analyzed for its duration, amplitude, and shape, enabling the identification of atrial abnormalities. The QRS complex was evaluated in terms of width, amplitude, and electrical axis to identify potential ventricular conduction issues. Abnormalities in the ST segment such as elevation or depression, suggest signs of myocardial ischemia or injury [40]. The T wave inversions or hyperacute peaks provided indicators of repolarization abnormalities [41]. To assess rhythm irregularities, RR intervals were computed for variability and arrhythmic patterns [42]. This comprehensive time-domain examination of raw ECG signals establishes a foundational basis for identifying a broad spectrum of cardiac pathologies, contributing to robust diagnostic decision-making [43].

2.5.2. Frequency Domain

The PQRST complex of the ECG signal was algorithmically transformed into the frequency domain to extract spectral features that may be imperceptible in the time domain. This transformation was performed primarily using Fast Fourier Transform (FFT) and wavelet-based decomposition techniques, which facilitated the identification of dominant frequency components associated with each segment of the cardiac cycle [44]. Frequency-domain features enabled the detection of subtle variations in spectral energy distributions. This may be indicative of early-stage cardiac abnormalities, such as conduction delays or ischemic conditions. Furthermore, the evaluation of R-R interval regularity in the

frequency domain enhanced the sensitivity to detecting minor arrhythmic patterns, which may not be evident in the raw ECG signal. Spectral analysis of the ST segment and T wave provided complementary diagnostic insights, particularly for identifying myocardial ischemia and repolarization instability [45].

2.5.3. Time-Frequency Domain

While time-domain analysis captures morphological variations in ECG signals and frequency-domain analysis reveals spectral energy distributions, both approaches individually fall short in preserving the dynamic temporal evolution of frequency content. To address this limitation, time-frequency domain feature extraction was employed, enabling simultaneous analysis of both time-localized and frequency-dependent signal characteristics. The ECG signal was segmented using a sliding window approach to track variations across key waveform components—the P wave, QRS complex, and T wave [46].

Each windowed segment underwent transformation using the Continuous Wavelet Transform (CWT) to generate scalogram images. It effectively illustrates how frequency content evolves over time [47]. This two-dimensional representation encodes both temporal localization and frequency scale resolution. It makes it suitable for capturing pathological variations in ECG morphology that are often subtle and nonstationary.

The resulting scalograms were treated as image-like inputs and processed using a two-dimensional Convolutional Neural Network (2D-CNN) to extract spatial patterns and texture information corresponding to time-frequency dynamics [48]. This approach facilitated the learning of both local and global features reflective of arrhythmic behavior, ischemic changes, or conduction abnormalities, especially in cases where traditional one-dimensional signal analysis might overlook such nuances [45].

2.6. Signal Visualization

To better understand the morphological and spectral characteristics of the ECG signals, Figure 7 presents representative visualizations across four classes, showing the transformation of the signal through successive stages: raw

input, denoised and filtered output, time-domain representation, frequency-domain (FFT) spectrum, and time-frequency (wavelet scalogram) representation. Although the raw and filtered signals exhibit only subtle variations across classes, these time-domain sequences retain essential morphological features such as P-QRS-T patterns, which are later exploited by the 1D-CNN. The filtered output ensures that noise and baseline wander are minimized to improve signal integrity. In contrast, the frequency-domain spectra provide clearer distinctions in the spectral energy distributions across classes, offering complementary information often undetected in the temporal dimension. The time-frequency representations generated via wavelet transforms capture both spectral and temporal evolution. Its patterns are suited for complex feature extraction by 2D-CNN architectures. The visualization of the ECG signals thus suggests that a single domain may be insufficient to fully capture the diagnostic variance in ECG signals, justifying the proposed multimodal fusion framework. Therefore, this work explores the complementarity of these different domains for a more generalized and accurate model.

Table 3 presents a tabulated insight and knowledge derived from the visualized ECG signals across multiple domains. Each row is a class showing a specific feature about the class. The feature type ranges from raw, time-domain data to complex time-frequency representations. It also highlights the corresponding transformation techniques used to process the signals. Furthermore, the table also shows clinical relevance of each datatype, the key advantages and inherent limitations associated with each transformation, offering a balanced view of their diagnostic potential and computational trade-offs. Finally, the use-case column grounds these features in real-world clinical applications. The proposed multimodal system leverages the synergistic collection of diverse strengths of the time, frequency and time-frequency domains to improve classification accuracy, robustness, and clinical interpretability.

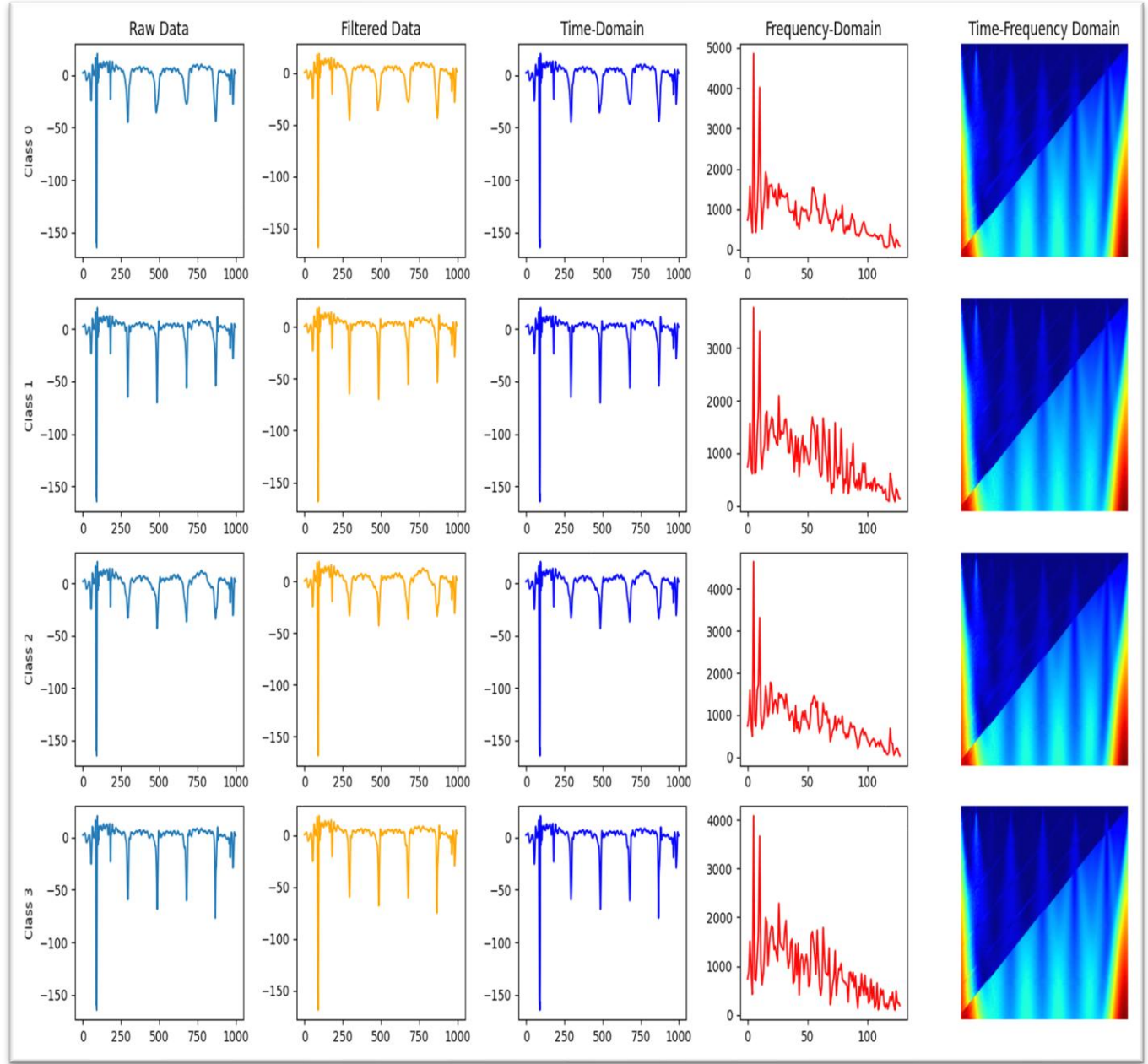


Figure 7. Multistage ECG Signal Preprocessing and Multi-Domain Feature Representation Across CVD Classes. The figure illustrates the sequential transformation of ECG signals for four representative cardiovascular disease (CVD) classes (Class 0–3), progressing from raw to multi-domain formats used in deep learning.

- **Column 1 (Raw Data):** Original ECG signals with baseline noise and artifacts.
- **Column 2 (Filtered Data):** Signals after Butterworth bandpass filtering to isolate clinically relevant frequency bands.
- **Column 3 (Time-Domain):** Clean waveforms capturing morphological features of PQRST complexes, used as input to 1D-CNN.
- **Column 4 (Frequency-Domain):** FFT-transformed signals highlighting dominant frequency components, fed to Transformer-based encoders.
- **Column 5 (Time-Frequency Domain):** Scalogram images derived via continuous wavelet transform, capturing both temporal and spectral features, used as input to 2D-CNNs.

Table 3. Clinical Significance of ECG Feature Representations

Feature Type	Transformation Method	Clinical Relevance	Advantages	Limitations	Use in Diagnosis
Raw Signal (Time-Domain)	Direct ECG waveform recording	Captures electrical activity of the heart in real-time	Provides complete information, easy for manual interpretation	Contains noise (e.g., baseline wander, powerline interference)	Used by cardiologists for arrhythmia detection, myocardial infarction diagnosis [49]
Filtered Signal (Time-Domain)	Bandpass filtering (e.g., 0.5–45 Hz)	Reduces noise while preserving cardiac waveform morphology	Improves signal clarity, enhances feature extraction	May remove clinically relevant low-frequency components	Enhances ECG quality for automated anomaly detection [50]
Time-Domain Features	Feature extraction (e.g., PQRST intervals, HRV, RR interval)	Captures morphological characteristics of ECG beats	Effective for detecting arrhythmias, simple to compute	Limited ability to detect frequency-based abnormalities	Used for heart rate variability (HRV) analysis, arrhythmia classification [51]
Frequency-Domain Features (FFT)	Fast Fourier Transform (FFT)	Identifies dominant frequency components of ECG signals	Detects periodic heart abnormalities, robust to noise	Loses temporal information requires careful interpretation	Used in atrial fibrillation (AFib) detection, ischemic heart disease screening [52]
Time-Frequency Features (Spectrograms)	Wavelet Transform, STFT, CWT	Represents transient cardiac events in both time and frequency domains	Captures complex and transient patterns, good for deep learning models	Computationally intensive, requires high-quality data	Used for diagnosing ventricular tachycardia, ischemia, and transient arrhythmias [53]

2.7. Fusion Strategies

Research question: Does the choice of fusion strategy (early, intermediate, or late) affect the classification performance of a multimodal deep learning architecture applied to an ECG dataset, considering the integration of time-domain, frequency-domain, and time-frequency domain features?

Answering the above question, this study seeks to determine the optimal fusion strategy for multimodal ECG classification using deep learning by systematically evaluating early, intermediate, and late fusion techniques. Each strategy is tested under multiple combinations of feature modalities derived from the time, frequency, and time-frequency domains, enabling a comprehensive assessment of their complementary and redundant contributions to classification performance.

2.7.1. Early Fusion

Early fusion involves the concatenation of features from multiple input domains at the initial stage of the model architecture prior to learning [54]. In this strategy, all extracted domain features are merged into a unified feature representation, which is then fed into a common neural network for classification. This approach ensures that the model learns from cross-domain interactions early in the learning pipeline.

In the context of ECG-based cardiovascular disease (CVD) classification, early fusion typically merges features from:

- **Time-domain signals** (1D waveforms),
- **Frequency-domain components** (e.g., FFT-transformed vectors), and
- **Time-frequency representations** (e.g., wavelet-based scalograms or spectrograms).

Because these modalities differ in shape and dimensionality, early fusion often requires extensive input reshaping and dimensional alignment. For example:

- A **binary fusion** might involve concatenating 1D time-domain features with 2D scalograms, which may necessitate flattening or projection into a shared latent space.
- A **ternary fusion** merges all three domains (time, frequency, time-frequency), requiring uniform representation before integration.

Figure 8 demonstrates an early fusion architecture of ECG signals, illustrating how diverse domain features are merged at the input level and processed through a shared neural pipeline.

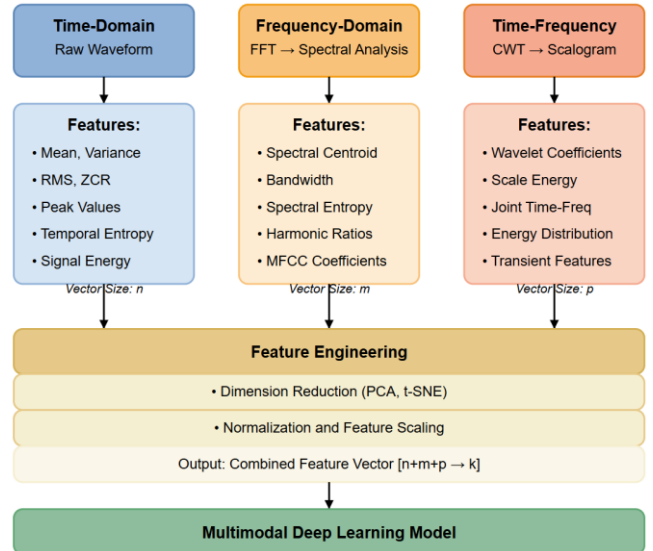


Figure 8. Early Fusion Strategy. The diagram depicts the logical process of ECG signal in an early fusion. Preprocessed signals are decomposed into time, frequency and time-frequency domains. At the fusion stage, domains are reshaped before fusion. Fused features are passed into a shared model for multimodal classification.

Early fusion acts as a valuable baseline for multimodal learning by offering insights into the combined feature space of ECG signals. By integrating raw or preprocessed features from multiple modalities at the input, early fusion enables the exploration of relationships and interactions between different modalities from the very beginning of model training. While it may be less advanced than intermediate or late fusion methods, it provides a simple framework for establishing initial performance benchmarks in multimodal ECG analysis.

2.7.2. Intermediate Fusion

Intermediate fusion, also referred to as feature-level fusion, represents a more sophisticated multimodal learning strategy where independent neural sub-networks are employed to extract high-level abstract features from each domain before integration. Unlike early fusion, which merges raw or preprocessed features at the input stage, intermediate fusion allows each modality to retain and refine its domain-specific characteristics through tailored processing pipelines prior to fusion [55].

Each domain is processed through a dedicated deep learning sub-network, such as:

- A **1D-CNN** for time-domain signal morphology,
- A **Transformer encoder** for frequency-domain spectral attention,
- A **2D-CNN** for spatial feature extraction from time-frequency images.

The outputs from these sub-networks are then concatenated, forming a unified intermediate representation, which is passed to a shared classification head composed of dense layers and a softmax output. This architectural design allows the model to learn complex inter-domain relationships without sacrificing modality-specific feature quality. Key advantages of intermediate fusion include:

- **Improved generalization** due to modular learning of features from different views of the ECG signal.
- **Higher accuracy and robustness**, particularly in multi-class classification of CVDs.
- Enhanced capacity for **interpretable modeling**, as each sub-network's contribution can be separately analyzed using explainable AI (XAI) tools like saliency maps.

The significant disadvantage of this fusion strategy is its complexity, requiring more computational resources [56]. However, rigorous hyperparameter tuning and balanced training of the sub-models may neutralize some of these setbacks. Figure 9 illustrates the intermediate fusion pipeline, showing independent domain-specific processing followed by a feature-level fusion layer and final decision layer.

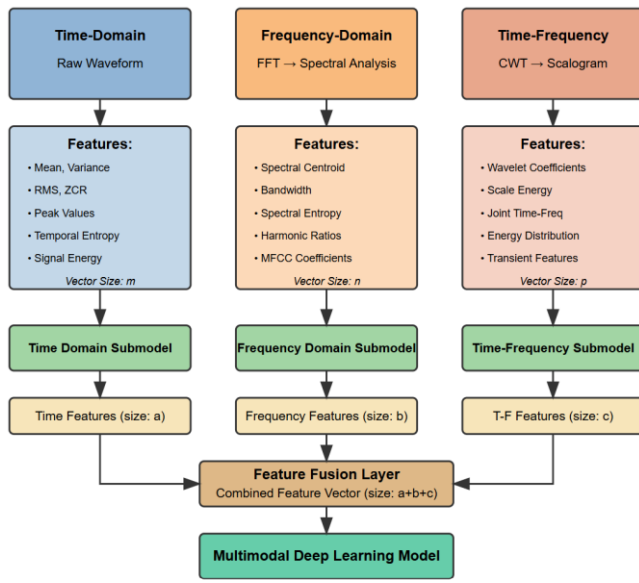


Figure 9. Intermediate Fusion Strategy. The diagram demonstrates an intermediate fusion approach in multimodal deep learning. Extracted features from time, frequency and time-frequency domains are further processed by individual submodels. Output from the submodels are fused together before a multimodal classification.

2.7.3. Late Fusion

Late fusion, also known as decision-level fusion, represents a modular and flexible approach where independent models are trained on each modality, and their predicted output (typically softmax probabilities) are later combined to make the final

classification decision. Unlike early and intermediate fusion, late fusion bypasses the need to reshape or integrate raw or intermediate features during training. Instead, each model operates in isolation, optimizing its own representation of the data modality [57]. The final class prediction is derived by aggregating the output probabilities from each model using a weighted averaging strategy. For example, if all 3 models (1D-CNN, 2D-CNN and Transformer) are to be fused

$$y'_{fused} = \alpha_1 \cdot y'_{1D-CNN} + \alpha_2 \cdot y'_{2D-CNN} + \alpha_3 \cdot y'_{Transformer} \quad (7)$$

where:

- $\alpha_1, \alpha_2, \alpha_3$ are optimized fusion weights,
- y'_{1D-CNN}, y'_{2D-CNN} and $y'_{Transformer}$ are the softmax probabilities from the individual models.

The weighted sum is followed by an argmax operation to determine the final predicted class label.

Figure 10 depicts the late fusion architecture, highlighting separate domain-specific branches and their final combination at the decision level.

Key Characteristics of Late Fusion:

- Simplicity in integration: Individual models can be developed, evaluated, and optimized independently.
- Modularity: Each branch can be swapped, retrained, or improved without retraining the entire system.
- Flexibility in domain contribution: Fusion weights can be adjusted based on validation accuracy or learned dynamically.

Limitations:

- The lack of joint feature learning may result in suboptimal performance compared to intermediate fusion, especially when cross-domain relationships are strong.
- Redundancy or dominance of a strong modality can skew the final decision if not carefully balanced.

Despite these limitations, late fusion has shown strong performance in various applications and provides a computationally efficient fallback when joint training is infeasible [58].

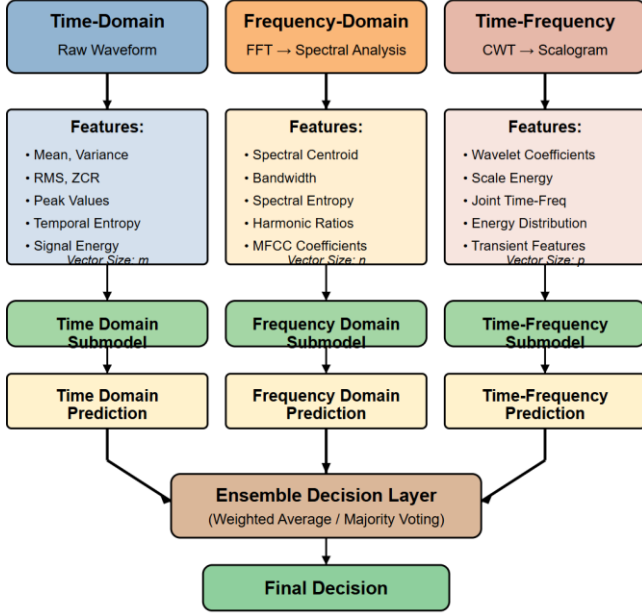


Figure 10. Late Fusion Strategy. In this framework, features are extracted independently from the time, frequency and time-frequency domains. Each domain is processed through a dedicated submodel that produces independent predictions. These domain-specific predictions are then aggregated—commonly using weighted averaging or majority voting—to form a final decision.

3. Experiment

Hypothesis

We hypothesize that multimodal data fusion across time, frequency, and time-frequency domains of ECG signals will significantly enhance predictive performance in cardiovascular disease (CVD) diagnosis compared to unimodal approaches. Furthermore, this fusion will facilitate greater clinical interpretability by elucidating the distinct contributions of each domain, while providing the development of more robust, explainable, and clinically aligned AI-driven diagnostic systems.

3.1. Unimodal Models

Three specific unimodal algorithms were designed:

- **Algorithm A:** 2D-CNN for the time-frequency domain
- **Algorithm B:** 1D-CNN for the time domain
- **Algorithm C:** 1D-CNN Transformer for the frequency domain.

A detailed exposition of Algorithms A, B, and C, including architecture and results, is presented in a related study [59]. Table 4 depicts the performance table.

Table 4. Unimodal Performance Table

Model	Accuracy	Precision	Recall	F1-Score
M1: 1D-CNN	0.94	0.94	0.94	0.94
M2: 2D-CNN	0.92	0.93	0.92	0.92
M3: Transformer	0.88	0.88	0.88	0.87

3.2. Early Fusion as a Baseline

To provide a fair comparison with intermediate and late fusion strategies, the early fusion is used as a baseline approach. Early fusion, or feature-level fusion, as described in Section 2.7.1, refers to the direct concatenation of feature representations from multiple modalities prior to classification [60]. Despite concerns regarding feature dilution due to unaligned or redundant features, the empirical performance of this approach was investigated using a deep Multilayer Perceptron (MLP). The experimental configuration for the fused Time, Frequency, and Time-Frequency domains is described in Figure 11. Unless otherwise specified, the hyperparameter values are their default values.

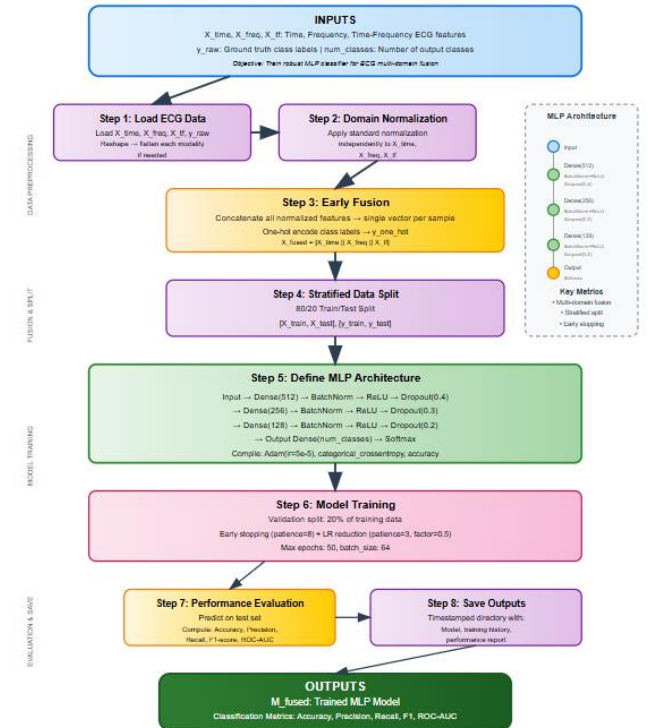


Figure 11. Early Fusion-Based Multilayer Perceptron (MLP) for Multidomain ECG Classification Configuration. This framework integrates features extracted from three complementary domains: time, frequency, and time-frequency into a unified feature representation. After independent normalization, the concatenated features are fed into an MLP consisting of

multiple dense layers with batch normalization and dropout for regularization. The model is trained using supervised learning with one-hot encoded labels and evaluated using standard classification metrics.

ECG signals were fused from the three domains: time-domain (X_time), frequency-domain (X_freq), and time-frequency representations (X_tf). All modalities were independently normalized before concatenation to preserve scale integrity. The fused representation was then passed through a deep multilayer perceptron (MLP) architecture with batch normalization, dropout regularization, and rectified linear unit (ReLU) activations. Table 5 summarizes the performance of different early fusion configurations evaluated using a deep MLP. The models fused features from two or three ECG domains (time, frequency, and time-frequency) and were evaluated using Accuracy, ROC-AUC, Macro F1-score, and Weighted F1-score.

As shown in Table 5, the early fusion MLP (Time + Time-Frequency) achieved an accuracy of up to 88.57% and a ROC-AUC of 0.9746 across several configurations. However, it was observed that adding more modalities (e.g., transitioning from two to three domains) did not significantly improve performance, suggesting saturation and potential feature redundancy. These findings reinforce the hypothesis that early fusion may suffer from feature dilution when combining heterogeneous representations, thereby motivating the design of more selective fusion mechanisms, such as intermediate and late fusion.

Consequently, early fusion serves as a crucial empirical baseline. The experiment demonstrates the limitations of this naive feature aggregation and provides a contrast to more complex fusion strategies that explicitly model inter-modal interactions.

Table 5. Performance Comparison of Early Fused Models

Model	Accuracy (%)	ROC-AUC	Macro Avg F1	Weighted Avg F1
Time + Time-Frequency	88.57	0.9746	0.88	0.88
Time + Frequency	88.00	0.9635	0.88	0.88
Time + Freq + Time-Freq	88.00	0.9645	0.88	0.88

While early fusion offers simplicity in implementation and a low-latency pipeline, it introduces several limitations:

- Feature-level fusion prior to domain-specific abstraction may lead to dilution of domain-specific patterns or interference among modalities.
- The approach lacks granular control over which domain contributes most to the prediction.
- The heterogeneity and misalignment of the different ECG signal domains (time, frequency and time-frequency) make fusion complex and potentially distorting information.
- Fusing domains together at the early stage can increase the dimensionality and complexity of the dataset. This raises concerns about computational cost and overfitting of the model.
- Early fusion is prone to noise which can impede the effectiveness of the model to learn necessary and sufficient features for an efficient CVD predictive model.

Given the challenges of early fusion, this study focuses on intermediate and late fusion techniques. These two approaches are strategically chosen because they offer more robust mechanisms for leveraging domain-specific learning, particularly in complex tasks such as multimodal learning [61]. By allowing each modality to be processed through dedicated pipelines before integration (intermediate fusion) or by combining decisions from independently trained models (late fusion), these strategies enhance the model's ability to capture and utilize complementary information from diverse data sources [62].

This work aims to empirically evaluate and compare models developed under intermediate and late fusion paradigms to determine the most effective strategy for ECG-based cardiovascular disease (CVD) classification. To ensure a rigorous assessment, experiments will be conducted to identify the best-performing model within each fusion category. The evaluation will be based on accuracy, precision, recall, and F1-score. The study intends to offer clear guidance on fusion design for real-world diagnostic applications by focusing on these fusion strategies. Statistical significance of model superiority will also be investigated. Figure 12 shows the experimental design of the study.

3.3. Intermediate Fusion Implementation

To implement intermediate fusion, learning algorithms were designed, trained and evaluated using fusion of features learned by the unimodal algorithms. By combining information after a learning algorithm has processed it, intermediate fusion exhibits greater robustness to noise [63].

Multi-Domain ECG Classification Experimental Design

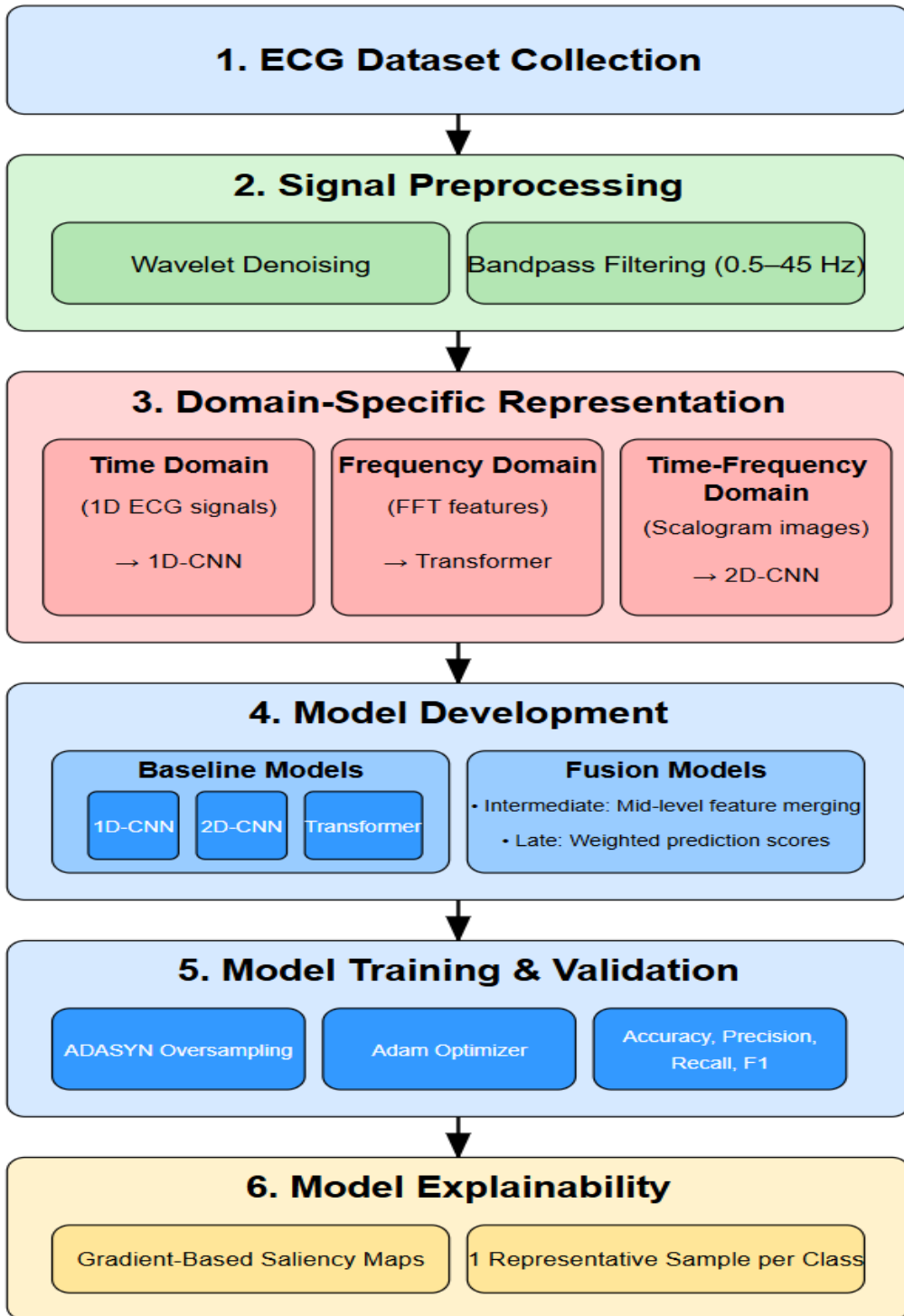


Figure 12. Overview of the experimental design for the multi-domain ECG signal classification. The experimental pipeline consists of six major stages: (1) ECG dataset collection; (2) signal preprocessing via wavelet denoising and bandpass filtering (0.5–45 Hz); (3) domain-specific representation, where time-domain signals are processed by a 1D-CNN, frequency-domain features (via FFT) are input to a Transformer, and time-frequency representations (scalograms) are analyzed using a 2D-CNN; (4) model development, including baseline models (1D-CNN, 2D-CNN, Transformer) and fusion strategies (intermediate and late fusion); (5) model training and validation using ADASYN for class balancing, the Adam optimizer, and evaluation metrics such as accuracy, precision, recall, and F1-score; and (6) model explainability using gradient-based saliency maps on one representative sample per class

The reduction of noise helps in mitigating overfitting, thereby improving the model's ability to generalize.

This experiment yielded four distinct intermediate fusion models:

- **M4:** Combining the learned features from the 1D-CNN (time domain) and the 1D-CNN Transformer (frequency domain). (**Algorithm B (features)** + **Algorithm C (features)**).
- **M5:** Combining the learned features from the 2D-CNN (time-frequency domain) and the 1D-CNN Transformer (frequency domain). (**Algorithm A (features)** + **Algorithm B (features)**)
- **M6:** Combining the learned features from the 1D-CNN (time domain) and the 2D-CNN (time-frequency domain). (**Algorithm A (features)** + **Algorithm C (features)**).
- **M7:** Combining the learned features from all three trained algorithms. (**Algorithm A (features)** + **Algorithm B (features)** + **Algorithm C (features)**)

Architectural details of intermediate fusion models are shown in Table 6. The experimental results are presented in both tabular and graphical forms in Table 7 and Figure 13, respectively. The experimental results of the intermediate fusion show that M4, a combination of a 1D-CNN trained on the time domain and a Transformer trained on the frequency domain, achieves the best performance. The worst-performing model was the M2, a 2D-CNN trained on time-frequency domain features.

Steps to implement the multimodal MD4: 1D + Transformer are shown in Algorithm 2. This algorithm is strategically chosen because it has the best performance during the implementation of all intermediate models. Unless otherwise specified, hyperparameter values are their default values.

Table 6. Intermediate Fusion Architecture

Model	Input Domains	Branch Components
M4: 1D + Transformer	Time (1D-CNN) Frequency (Transformer)	1D-CNN: Conv1D → ReLU → Pool → BatchNorm → Flatten Transformer: FFT → Positional Encoding → MHA → FFN → Flatten
M5: 2D + Transformer	Time-Frequency (2D-CNN) Frequency (Transformer)	2D-CNN: Conv2D → ReLU → Pool → Flatten Transformer: FFT → MHA → FFN → Flatten
M6: 1D + 2D CNN	Time (1D-CNN) Time-Frequency (2D-CNN)	1D-CNN: Conv1D → ReLU → Pool → Flatten 2D-CNN: Conv2D → ReLU → Pool → Flatten

M7: 1D + 2D + Transformer	Time (1D-CNN) Time-Frequency (2D-CNN) Frequency (Transformer)	1D-CNN: Conv1D → Pool → Flatten → Dense 2D-CNN: Conv2D → Pool → Flatten → Dense Transformer: FFT → Positional Encoding → MHA → FFN → Flatten
----------------------------------	---	--

Algorithm 2: Intermediate Fusion Model (MD4: 1D-CNN + Transformer)

Inputs:

M_ID, M_Trans : Pretrained 1D-CNN and Transformer models

X_ID, X_FFT : Time-domain and Frequency-domain data

y_train, y_test : Ground truth class labels

$num_classes$: Total number of output classes

Outputs:

M_fused : Trained hybrid model

Classification metrics: Accuracy, Precision, Recall, F1-score

Steps:

1. Load and preprocess training data:
 - Load X_ID, X_FFT, y_train
 - Reshape:
 - $X_ID \rightarrow (N, 1000, 1)$
 - $X_FFT \rightarrow (N, 128, 1)$
 - Align all arrays to equal length
 - Encode y_train to one-hot vectors → y_train_cat
2. Split into training and validation:
 - Perform stratified 80/20 split:
 - $[X_train_ID, X_val_ID], [X_train_FFT, X_val_FFT], [y_train_cat, y_val_cat]$
3. Restore pretrained models:
 - Load M_ID and M_Trans
 - Set $M_ID.trainable \leftarrow True$
 - Set $M_Trans.trainable \leftarrow True$
4. Build intermediate fusion model:
 - Define $input_ID \leftarrow Input(shape=(1000, 1), name="ID_ECG")$
 - Pass through $M_ID \rightarrow Flatten \rightarrow Dense(256, ReLU) \rightarrow BatchNormalization \rightarrow x1$
 - Define $input_FFT \leftarrow Input(shape=(128, 1), name="Transformer_ECG")$
 - Pass through $M_Trans \rightarrow Flatten \rightarrow Dense(256, ReLU) \rightarrow BatchNormalization \rightarrow x2$
 - $Concatenate(x1, x2) \rightarrow merged$
 - $Dense(512, ReLU) \rightarrow BatchNormalization \rightarrow Dropout(0.25) \rightarrow output$

- Build $M_{fused} \leftarrow Model([input_ID, input_FFT], output)$

- Compile M_{fused} with:

Optimizer $\leftarrow Adam(learning_rate=3e-5)$

Loss $\leftarrow categorical_crossentropy$

Metric $\leftarrow accuracy$

5. Train M_{fused} :

- Use early stopping on val_loss with patience=10

- Fit model on:

Inputs: $[X_train_ID, X_train_FFT]$

Labels: y_train_cat

Validation: $([X_val_ID, X_val_FFT], y_val_cat)$

Epochs: 60

Batch size: 32

6. Evaluate performance:

- Load and preprocess X_test_ID and X_test_FFT

- Predict: $y_pred \leftarrow$

$argmax(M_{fused}.predict([X_test_ID, X_test_FFT]))$

- Compute metrics:

Accuracy, Precision (weighted), Recall (weighted),

F1-score (weighted)

7. Return:

Trained model M_{fused} and classification report

EndAlgorithm

Table 7. Performance Comparison Table of Intermediate Fusion Models

Model	Accuracy	Precision	Recall	F1-Score
M4: 1D + Transformer	0.97	0.97	0.97	0.97
M5: 2D + Transformer	0.89	0.90	0.89	0.89
M6: 1D + 2D CNN	0.95	0.95	0.95	0.95
M7: 1D + 2D + Transformer	0.95	0.95	0.95	0.95

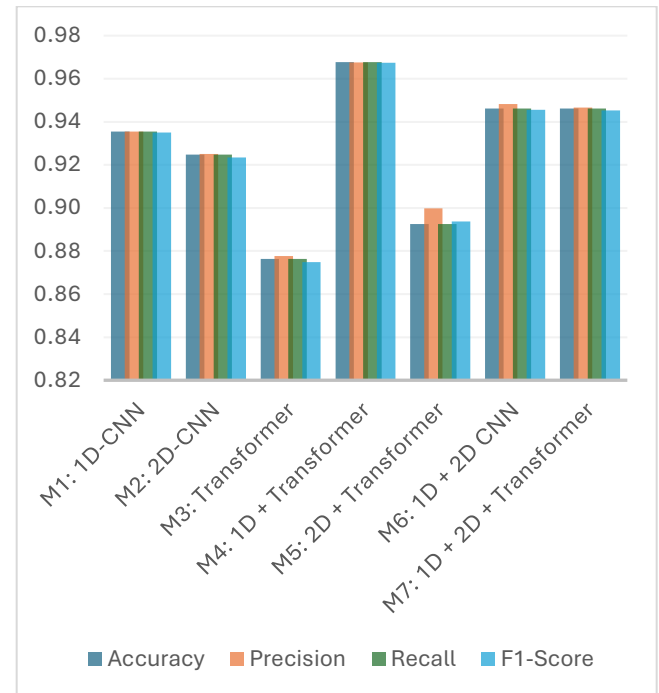


Figure 13. Performance comparison of all evaluated models (M1–M7) across four classification metrics: accuracy, precision, recall, and F1-score. M4 (1D-CNN + Transformer), representing intermediate fusion, achieved the highest scores across all metrics, outperforming both unimodal models (M1: 1D-CNN, M2: 2D-CNN, M3: Transformer) and other hybrid models. M6 and M7, which integrate two and three modalities, respectively, show improved performance over individual models, particularly M7 (1D + 2D + Transformer), which demonstrates robust generalization and balanced classification performance. These results support the effectiveness of multimodal fusion strategies.

3.3.1. Late Fusion Implementation

Late fusion was implemented by aggregating the prediction probabilities of independently trained unimodal models using a weighted averaging scheme [64]. The goal was to determine sets of fusion weights that maximize the overall classification performance of the combined model. An exhaustive approach using the grid search technique was employed by systematically exploring combinations of weights across the prediction vectors. This method is widely used in multimodal fusion literature due to its simplicity and effectiveness in identifying near-optimal fusion parameters without requiring gradient-based optimization [65, 66]. The resulting fused model benefited proportionally from the complementary strengths of the individual modalities, enhancing robustness and diagnostic accuracy in ECG signal classification [67] [3].

The specific steps for late fusion in this study were:

- Train individual base models on their respective input domains:

- A 2D Convolutional Neural Network (2D-CNN) trained on scalogram image (Algorithm A)
- A 1D Convolutional Neural Network (1D-CNN) trained on time-domain data (Algorithm B)
- A Transformer network trained on Fast Fourier Transform (FFT) signals (Algorithm C)
- For each test sample, the softmax output (probability distribution over classes) from each trained model was saved:
 - 1D-CNN saved as `y_pred_1d.npy`.
 - 2D-CNN saved as `y_pred_2d.npy`.
 - Transformer saved as `y_pred_transformer.npy`,
- The final prediction for each sample was obtained by calculating a weighted sum of these saved softmax outputs.
- A grid search technique was used to systematically explore different combinations of weights (α) to identify the set of weights that resulted in the best overall performance of the fused model.
- This optimization process was conducted exclusively on the independent validation dataset to prevent data leakage and mitigate the risk of overfitting the fusion weights. Once the optimal weights were determined based on their performance on the validation set, these fixed weights were then applied to the completely unseen test dataset for the final performance evaluation of the late fusion models (e.g., M7).
- The rigorous separation ensures that the reported performance metrics for late fusion models accurately reflect their generalization capabilities on new, unobserved data.

Architectural details of the Late Fusion models are shown in Table 8. Figures 14 to 17 show the grid search graph for the optimal fusion of the models. Experimental results are presented in Table 9 and Figure 17, in both tabular and graphical representations. The results indicate that M7: 1D-CNN + 2D-CNN + Transformer achieves the best performance. M5: 1D-CNN + Transformer and M6: 2D-CNN + Transformer are tied for the worst performance. Algorithm 3 outlines the logical steps for implementing M7. This algorithm was strategically chosen because it has the best performance during implementation. Unless otherwise specified in the algorithm, hyperparameter values are their default values.

Table 8. Late Fusion Architecture

Model	Modalities Used	Architecture Description

M4: 1D-CNN + 2D-CNN	Time + Time-Frequency	Classification probabilities from each model are aggregated: $\hat{y} = \alpha_1 \hat{y}_{1D} + \alpha_2 \hat{y}_{2D}$ $\alpha_1 = 0.7, \alpha_2 = 0.3$
M5: 1D-CNN + Transformer	Time + Frequency	Independent predictions from 1D-CNN and Transformer. Final decision based on weighted averaging: $\hat{y} = \alpha_1 \hat{y}_{1D} + \alpha_2 \hat{y}_{\text{Transformer}}$ $\alpha_1 = 0.6, \alpha_2 = 0.4$
M6: 2D-CNN + Transformer	Time-Frequency + Frequency	Softmax outputs from 2D-CNN and Transformer are combined: $\hat{y} = \alpha_1 \hat{y}_{2D} + \alpha_2 \hat{y}_{\text{Transformer}}$ $\alpha_1 = 0.7, \alpha_2 = 0.3$
M7: 1D-CNN + 2D-CNN + Transformer	Time + Time-Frequency + Frequency	All three models predict independently. Final prediction is derived from: $\hat{y} = \alpha_1 \hat{y}_{1D} + \alpha_2 \hat{y}_{2D} + \alpha_3 \hat{y}_{\text{Transformer}}$ $\alpha_1 = 0.3, \alpha_2 = 0.3, \alpha_3 = 0.4$

Notably, to avoid overfitting during fusion weight optimization, the grid search was conducted exclusively on a validation subset derived from the training data. The final performance metrics, including accuracy, precision, recall, and F1-score, were evaluated on an independent test set held out throughout training and fusion tuning. This separation ensures that the reported improvements reflect the model's generalization performance rather than validation bias.

Algorithm 3: Multimodal Weighted Late Fusion (M7: 1D-CNN + 2D-CNN + Transformer)

Inputs:

$M_{1D}, M_{2D}, M_{\text{Trans}}$: Trained 1D-CNN, 2D-CNN, and Transformer models (From Algorithms A, B, and C)

$X_{1D}, X_{2D}, X_{\text{FFT}}$: Time, Time-Frequency, and

Frequency-domain test data

y_{true} : Ground truth class labels

$\alpha_i \in [0.0, 1.0]$ such that $\alpha_1 + \alpha_2 + \alpha_3 = 1$

Outputs:

Optimal weights ($\alpha_1^*, \alpha_2^*, \alpha_3^*$)

Best classification metrics: Accuracy, Precision, Recall, F1-score

Steps:

1. Load trained models:

$M1D \leftarrow M_{1D}$

$M2D \leftarrow M_{2D}$

$MTrans \leftarrow M_{\text{Trans}}$

2. Load and align test inputs:

Load $X_{1D}, X_{2D}, X_{\text{FFT}}, y_{\text{true}}$

Ensure all inputs have equal sample length

3. Predict class probabilities from each model:

$$\begin{aligned}\hat{Y}_{ID} &\leftarrow M1D(X_{ID}) \\ \hat{Y}_{2D} &\leftarrow M2D(X_{2D}) \\ \hat{Y}_{Trans} &\leftarrow MTrans(X_{FFT})\end{aligned}$$

4. Initialize empty list: $results \leftarrow []$

5. For α_1 in $[0.0, 0.05, \dots, 1.0]$:

6. For α_2 in $[0.0, 0.05, \dots, 1.0]$:

$$\alpha_3 \leftarrow 1.0 - \alpha_1 - \alpha_2$$

8. If $\alpha_3 \in [0.0, 1.0]$:

$$9. \hat{Y}_{fused} \leftarrow \alpha_1 \cdot \hat{Y}_{ID} + \alpha_2 \cdot \hat{Y}_{2D} + \alpha_3 \cdot \hat{Y}_{Trans}$$

$$10. y_{pred} \leftarrow \text{argmax}(\hat{Y}_{fused}, \text{axis}=1)$$

11. Compute metrics: Accuracy, Precision,

Recall, F1-score

12. Append $(\alpha_1, \alpha_2, \alpha_3, \text{Accuracy}, \text{Precision}, \text{Recall}, \text{F1 score})$ to results

13. Select the tuple with the best Accuracy:

$$(\alpha_1^*, \alpha_2^*, \alpha_3^*, \text{Acc}^*, \text{Prec}^*, \text{Rec}^*, \text{F1}^*) \leftarrow \text{argmax}(\text{results})$$

14. Return optimal weights and evaluation metrics

EndAlgorithm

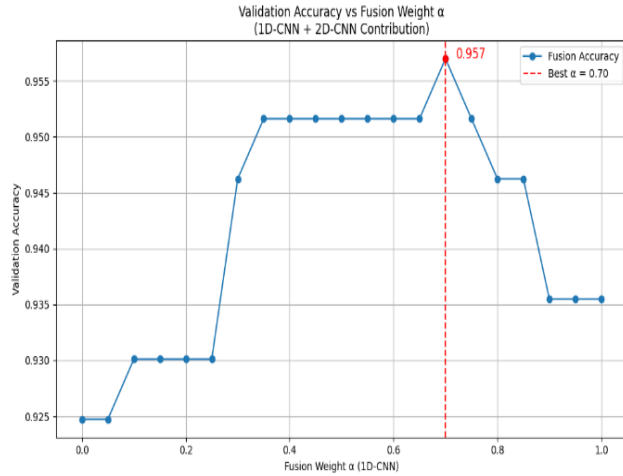


Figure 14. M4: 1D-CNN + 2D-CNN. The fusion weight α is adjusted to control the contribution of the 1D-CNN branch relative to the 2D-CNN. Here, $\alpha \in [0, 1]$ represents the proportion of the final prediction attributed to the 1D-CNN, with the remaining $(1 - \alpha)$ from the 2D-CNN branch. The highest validation accuracy of 0.957 is obtained at $\alpha = 0.70$, highlighted by the red dashed line, indicating that the model benefits most when the 1D-CNN's time-domain features are moderately prioritized over the time-frequency features captured by the 2D-CNN. This result highlights the synergistic value of both domains while affirming the dominance of time-domain signals in achieving higher classification accuracy.

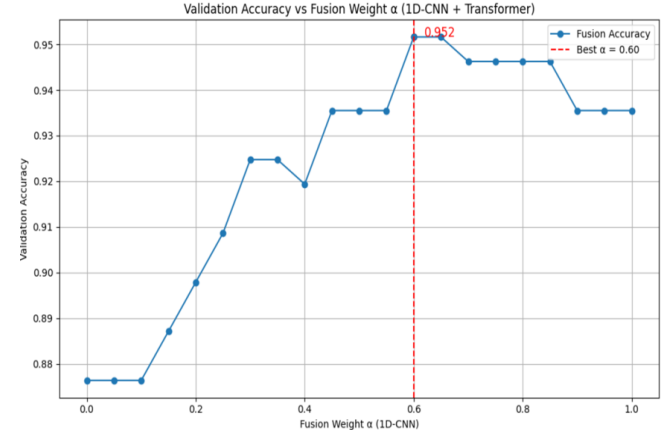


Figure 15. M5 : 1D-CNN + Transformer. The fusion weight $\alpha \in [0, 1]$ controls the relative contribution of the 1D-CNN prediction in the final decision: $\alpha = 0$ uses only the Transformer output, while $\alpha = 1$ uses only the 1D-CNN. The plot shows that the optimal accuracy (0.952) is achieved at $\alpha = 0.60$, as indicated by the red vertical dashed line. This suggests that assigning a slightly higher weight to the 1D-CNN output improves the overall classification performance, confirming that the CNN captures critical time-domain patterns that complement the frequency-based representations from the Transformer.

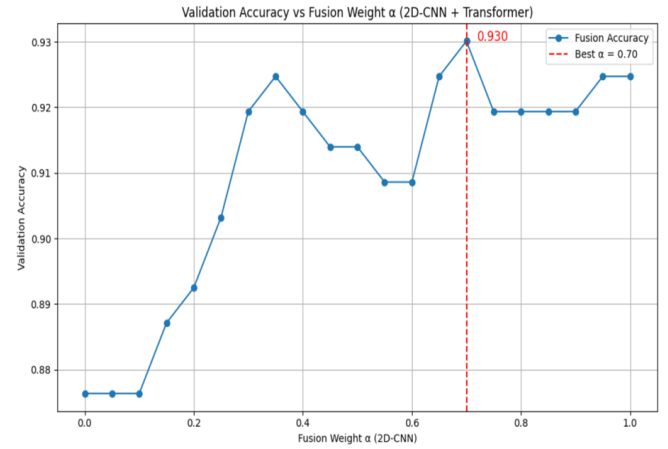


Figure 16. M6 : 2D-CNN + Transformer. The fusion weight $\alpha \in [0, 1]$ controls the proportion of the final prediction influenced by the 2D-CNN, with $(1 - \alpha)$ contributed by the Transformer. The highest validation accuracy of 0.930 occurs at $\alpha = 0.70$, as indicated by the red dashed line. This result implies that giving greater emphasis to time-frequency domain features extracted by the 2D-CNN improves performance more than relying solely on the Transformer's frequency-based representations. The overall trend underscores the complementary role of domain-specific features and the effectiveness of learned weighting in late-stage decision fusion.

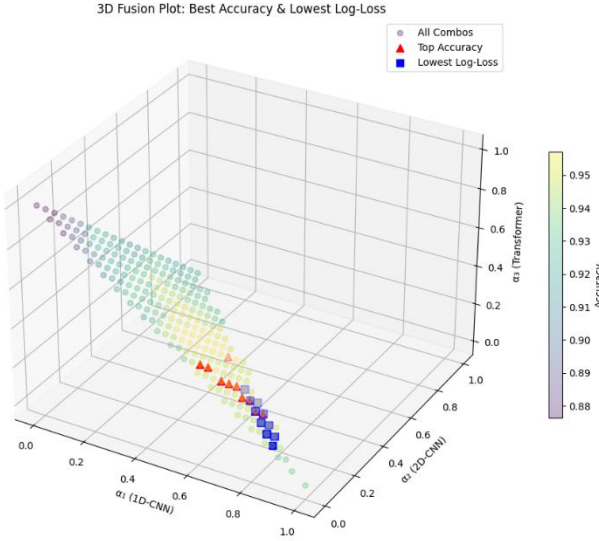


Figure 17. M7 :1D-CNN + 2D-CNN + Transformer. 3D Visualization of fusion weight combinations (α_1 : 1D-CNN, α_2 : 2D-CNN, α_3 : Transformer) and their corresponding classification accuracies. The optimal validation accuracy of 0.96 is attained when the α_1 values of 1D-CNN (Time domain), 2D-CNN (Time-Frequency domain) and Transformer (Frequency domain) are 0.3, 0.3 and 0.4 respectively. Each point represents a unique combination of weights summing to 1. Color intensity indicates classification accuracy, with warmer tones representing higher accuracy. Red triangles highlight combinations achieving top accuracy, while blue squares mark combinations with the lowest log-loss, reflecting better model confidence.

Table 9. Performance Comparison Table of Late Fusion Models

Model	Accuracy	Precision	Recall	F1-Score
1D + 2D	0.94	0.94	0.94	0.94
1D + Transformer	0.93	0.94	0.93	0.93
2D + Transformer	0.93	0.93	0.93	0.93
1D + 2D + Transformer	0.96	0.96	0.96	0.96

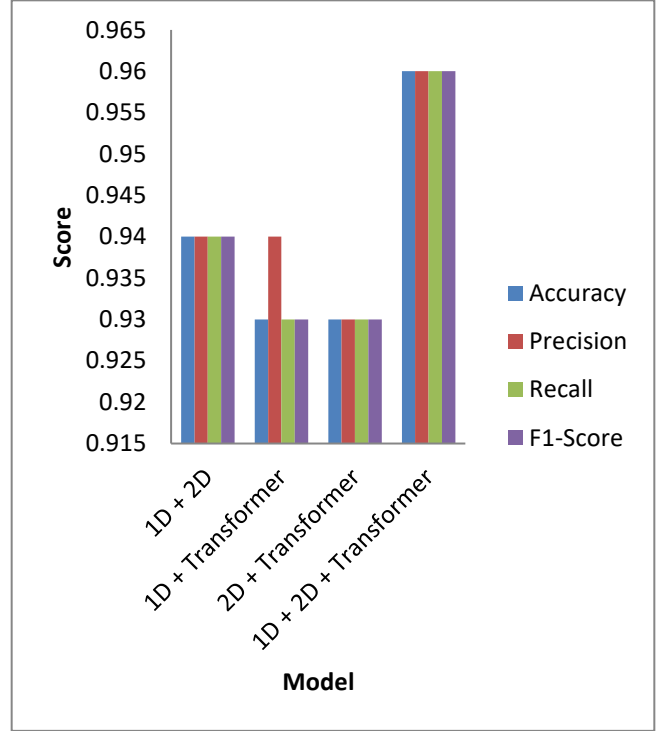


Figure 18. Comparison of performance metrics—accuracy, precision, recall, and F1-score—across four hybrid ECG classification models: 1D + 2D CNN, 1D-CNN + Transformer, 2D-CNN + Transformer, and the full multimodal fusion model (1D + 2D + Transformer). The superiority of the 1D + 2D + Transformer model demonstrates the benefit of integrating temporal, spectral, and time-frequency domain features.

4. DISCUSSION

Figure 19 summarizes the framework used to structure the multimodal ECG classification study. The experimental workflow was organized into three sequential stages: (i) modality extraction, (ii) fusion strategy design, and (iii) derivation of key findings. The first stage comprises three distinct domains: the time domain, the frequency domain, and the time-frequency domain. These modalities were selected to capture different signal characteristics: temporal morphology, spectral composition, and localized time-frequency variations. The second stage of the experiment focused on implementing various fusion strategies. This includes early, intermediate, and late fusion each designed to evaluate how the integration depth of modalities affects classification performance. Also included were multiple model architectures to systematically explore modality complementarity, redundancy, and synergy. To identify the optimal fusion approach, a comparative analysis was conducted between the highest-performing models from each strategy.

Figure 20 highlights the architectural comparison between the best intermediate fusion model (M4: 1D-CNN +

Transformer) and the best late fusion model (M7: 1D-CNN + 2D-CNN + Transformer).

In M4, the latent feature representations extracted from the 1D-CNN (which captures temporal features) and the Transformer (which captures frequency-based dependencies through self-attention) were concatenated to form a unified representation. This fused feature vector was then fed into a fully connected classification head, allowing the model to learn joint representations and optimize decision boundaries using combined temporal-spectral information.

In contrast, M7 adopts a late fusion strategy wherein each modality is processed independently: the 1D-CNN learns from raw temporal sequences, the 2D-CNN processes time-frequency scalograms, and the Transformer models frequency-domain representations. Each branch produces an independent softmax prediction. These predictions were then aggregated using a weighted summation, where the contribution of each modality is controlled by learned or manually tuned weights. While this design allows for modularity and model specialization, it does not exploit joint feature interactions across modalities, which may limit its capacity to capture higher-order cross-domain dependencies. This study deliberately adopted the weighted fusion approach for M7, as it enables selective emphasis on more informative modalities, rather than using uniform averaging which may suppress dominant signal cues.

The performance comparison presented in Figure 20 supports the hypothesis that intermediate fusion (as implemented in M4) more effectively captures complementary features and leads to improved classification performance over late fusion (M7), particularly in the context of complex ECG signal variability across CVD classes.

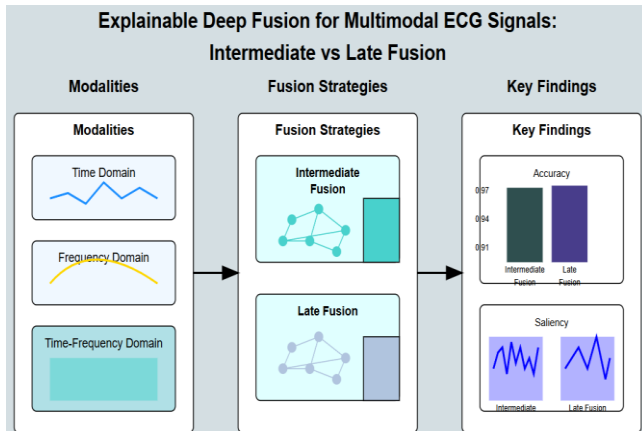


Figure 19. Architectural model comparison diagram illustrating the framework and findings of the experiment. The left panel outlines the modalities (time, frequency and time-frequency domains). The center panel presents the two fusion strategies explored—intermediate fusion and late fusions. Keys findings are

in the right panel for model performance and interpretability with Saliency maps.

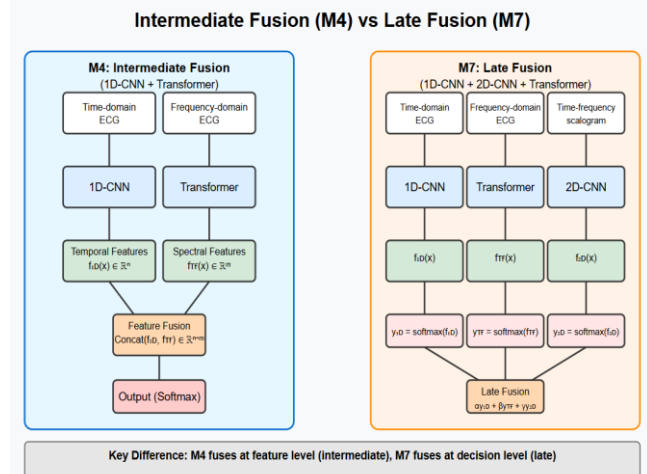


Figure 20. Best Intermediate Fusion (M4) VS Best Late Fusion (M7). In M4, time-domain and frequency-domain ECG signals are processed by a 1D-CNN and a Transformer, respectively, and their latent features are concatenated before the classification layer, enabling feature-level integration. In M7, the three modalities (time, frequency, and time-frequency) are independently processed by 1D-CNN, Transformer, and 2D-CNN models respectively. The key distinction lies in fusion depth: M4 performs early integration of informative representations, whereas M7 combines post-classification probabilities.

4.1. Training Configuration and Reproducibility

All models (unimodal and multimodal) in this study were implemented in Python using the Keras deep learning library with a TensorFlow backend. Unless otherwise noted, training was performed using the Adam optimizer ($\beta_1 = 0.9$, $\beta_2 = 0.999$, $\epsilon = 1e-7$) with an initial learning rate of 0.001 and a batch size of 64. A learning rate schedule was applied using Keras’s LearningRateScheduler callback to reduce the rate by a factor of 0.1 every 10 epochs. Training ran for a maximum of 100 epochs, with early stopping based on validation loss (patience = 10) and automatic restoration of the best weights. The source code will be released on GitHub upon manuscript acceptance to support transparency and reproducibility.

4.2. Theoretical Premises (Mathematical Statements)

Let:

X_{TD} : Time domain features (1DCNN)

Z_{TD} : Latent Space for 1DCNN

f_{ID} : $X_{TD} \rightarrow Z_{TD}$

X_{FD} : Frequency domain features (Transformer)

Z_{FD} : Latent Space for Transformer

F_{FD} : $X_{FD} \rightarrow Z_{FD}$

X_{TFD} : Time-Frequency domain features (2DCNN)

Z_{TFD} : Latent Space for 2DCNN

F_{TFD} : $X_{TFD} \rightarrow Z_{TFD}$

\hat{Y}_1 : Prediction from the 1DCNN

\hat{Y}_2 : Prediction from the 2DCNN
 \hat{Y}_3 : Prediction from the Transformer
 \hat{Y}_{LT} : Final Prediction from the Late Fusion
 \hat{Y}_{IT} : Final Prediction from the Intermediate Fusion
 Y : Target
 g_{IT} : Intermediate Fusion Classifier
 $I(A, B)$: Mutual information between A and B
 h_{IT} : Intermediate Fusion Transformation
 f : a combined function

4.2.1. M4: 1DCNN + Transformer (Best Intermediate)

- Fusion Layer:

$$h_{IT}: Z_{TD} \times Z_{FD} \rightarrow Z_{IT_}^{fused}$$

- Classification:

The fused representation is passed through a classifier

$$g_{IT}: Z_{IT_}^{fused} \rightarrow \hat{Y}_{IT}$$

- Information Theoretic Perspective:

$$I(Y; \hat{Y}_{IT}) \leq I(Y; Z_{IT_}^{fused})$$

- If joint information of Z_{ID} and Z_{FD} are required to predict \hat{Y} , then,
 - $I(Y; Z_{ID}, Z_{FD}) > I(Y; Z_{ID})$
 - $I(Y; Z_{ID}, Z_{FD}) > I(Y; Z_{FD})$
- For an optimized intermediate fusion $Z_{IT_}^{fused}$
 - $I(Y; g_{IT}(h_{IT}(Z_{ID}, Z_{FD}))) = I(Y; Z_{ID}, Z_{FD})$
- In practice, due to model capacity and training limitations, the achieved mutual information will be:
 - $I(Y; Z_{IT_}^{fused}) \approx I(Y; Z_{ID}, Z_{FD}) - \epsilon$
 - where $\epsilon \geq 0$ represents the information loss during the fusion and classification process

4.2.2. M7: 1D + 2D + Transformer (Best Late)

- Independent modeling:

Each subnet produces an independent prediction:

$$\begin{aligned} Z_{TD} &\rightarrow \hat{Y}_1 \\ Z_{TFD} &\rightarrow \hat{Y}_2 \\ Z_{TF} &\rightarrow \hat{Y}_3 \end{aligned}$$

- Fusion at Decision Level:

$$\hat{Y}_{LT} = \sum_i w_i \cdot \hat{Y}_i$$

- Information Theoretic Interpretation:

$$I(Y; \hat{Y}_{IT}) \leq f(I(Y; \hat{Y}_1), I(Y; \hat{Y}_2), I(Y; \hat{Y}_3))$$

Figure 21 presents the comparative performance of the best intermediate and late fusion strategies using Accuracy,

Precision, Recall, and F1-score as evaluation metrics. The results clearly show that the best intermediate fusion model, M4 (1D-CNN + Transformer), consistently outperforms the best late fusion model, M7 (1D + 2D + Transformer). This superior performance of M4 may be attributed to its fusion strategy, which operates at the feature level. By jointly learning from temporal (1D-CNN) and spectral (Transformer) latent representations prior to classification, M4 can capture richer, more complementary information. The concatenation of these latent embeddings enables the model to form a more expressive joint representation, which enhances class separability and reduces ambiguity during classification.

In contrast, M7 applies fusion at the decision level, where each modality-specific model (1D, 2D, Transformer) makes an independent prediction, and the final decision is derived through weighted aggregation. Most likely, M7 might not have benefited from synergistic relationship among the models. Therefore, the advantage of M4 stems from its ability to perform deep integration of modalities during feature learning, resulting in better generalization and improved clinical prediction accuracy.

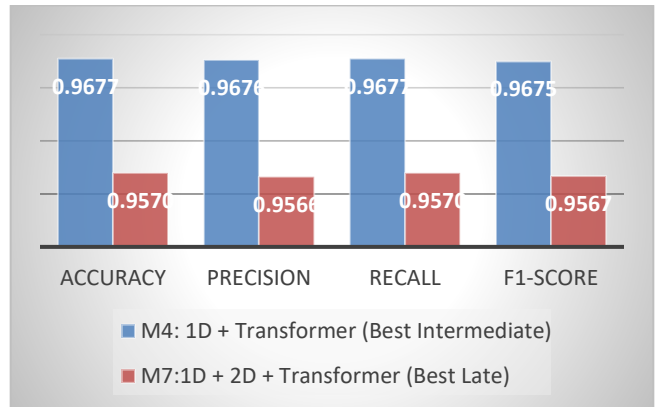


Figure 21. Comparison of classification performance between the best intermediate fusion model (M4: 1D-CNN + Transformer) and the best late fusion model (M7: 1D + 2D + Transformer) across accuracy, precision, recall, and F1-score metrics. The intermediate fusion model (M4) consistently outperforms the late fusion model (M7) in all evaluated metrics, achieving the highest accuracy (0.9677), precision (0.9676), recall (0.9677), and F1-score (0.9675). These results underscore the superior discriminative capability of intermediate fusion in integrating complementary ECG domain representations.

4.3. Noise Robustness Evaluation for M4: 1DCNN + Transformer (Best Intermediate)

Research Question: Can the intermediate fusion model (M4: 1D-CNN + Transformer) maintain satisfactory performance (F1-score) when subjected to independent

injections of Gaussian noise (15 dB SNR), baseline wander (0.15 Hz), and muscle noise (20–50 Hz), thereby demonstrating its robustness for practical ECG classification?

To evaluate the robustness of the intermediate fusion model (M4: 1D-CNN + Transformer) against real-world ECG signal disturbances, a controlled ablation study was performed by introducing three types of clinically relevant noise into the test dataset. These selected noise types represent common artifacts seen in ambulatory ECG recordings.

- Gaussian noise to simulate environmental interference (15 dB SNR) [68].
- Baseline wander to emulate motion-induced signal drift (0.15 Hz) [69].
- Muscle noise to capture high-frequency electrical activity from muscle contractions (20–50 Hz) [70].

Each noise condition was tested separately, and model performance was re-evaluated using the F1-score to measure degradation compared to clean test data. This experiment mimics real-world deployment scenarios, where model robustness against signal corruption is essential for clinical reliability. The steps to carry out noise evaluation in the proposed model (M4) are detailed in Algorithm 4.

Algorithm 4: Noise Robustness Evaluation for M4

Inputs:

M_4 : Pretrained intermediate fusion model (1D-CNN + Transformer)

X_{test} : Clean ECG test samples

y_{test} : Ground truth class5 labels

fs : Sampling frequency

Outputs:

$F1_{clean}$: Baseline F1-score under clean condition

Δ : Degradation from clean baseline across noise types

Steps:

1. Define ECG noise types:

$noise_types \leftarrow \{Gaussian, BaselineWander, Muscle\}$

2. Predict on clean test data:

$\hat{y}_{clean} \leftarrow M_4(X_{test})$

$F1_{clean} \leftarrow F1_score(y_{test}, \hat{y}_{clean})$

3. Initialize results $\leftarrow []$

4. For $noise_type$ in $noise_types$:

5. $X_{noisy} \leftarrow ApplyNoise(X_{test}, noise_type, fs)$

6. $\hat{y}_{noise} \leftarrow M_4(X_{noisy})$

7. $F1_{noise} \leftarrow F1_score(y_{test}, \hat{y}_{noise})$

8. $\Delta \leftarrow F1_{noise} - F1_{clean}$

9. Append ($noise_type$, $F1_{noise}$, Δ) to results

10. Return:

F1_clean, results

EndAlgorithm

The results of implementing the above algorithm are shown in Table 10.

Table 10. Robustness of M4 to Noise Injection

Noise Type	F1-score	Δ from Clean (%)
Clean (baseline)	0.963	—
Gaussian Noise (15 dB)	0.942	-2.18%
Baseline Wander	0.934	-3.01%
Muscle Noise	0.926	-3.84%

As shown in Table 10, the results indicate that M4 maintains relatively high performance across all noise conditions, with F1-score reductions staying below 4%. This supports the model's potential for deployment in real-world ECG monitoring scenarios, where noise contamination is common. Among the tested artifacts, muscle noise caused the most significant performance drop (-3.84%), suggesting that future research could explore data augmentation or adaptive filtering to improve robustness further.

4.4. Cohen's d Comparison of Intermediate and Late Fusion Models vs. Standalone Baselines for ECG Classification

Research Question: To what extent does intermediate fusion (M4) significantly outperform unimodal and late fusion models (M7) in ECG-based cardiovascular disease classification, as measured by Cohen's d, and performance metrics such as F1-score, accuracy, and precision?

The superior performance of fused models, both intermediate and late fusion, over their unimodal counterparts is consistently highlighted across all evaluation metrics. The empirical results support the hypothesis that multimodal fusion boosts the performance of deep learning models compared to models trained on single domains. To statistically confirm these performance improvements further, Cohen's d was calculated, revealing that the differences between fused and unfused models are statistically significant. Additionally, a comparison was made between the top-performing late fusion model and the best intermediate fusion model to determine which one is empirically dominant. The results indicate that multimodal fusion, especially when performed through intermediate or late integration, significantly enhances classification accuracy, robustness, and clinical reliability in ECG signal interpretation. [71, 72].

Effect size analysis using Cohen's d provides a robust and interpretable statistical measure for evaluating the practical significance of observed differences in model performance. While conventional metrics such as accuracy and F1-score indicate predictive effectiveness, Cohen's d quantifies the magnitude of performance improvement between fusion-based models and their unimodal counterparts, independent of sample size [73]. This distinction is fundamental in clinical machine learning, where statistically significant improvements must also demonstrate meaningful effect sizes to justify their application in sensitive diagnostic environments [74].

Each fusion model was compared against standalone models built on individual modalities (1D-CNN for time-domain, 2D-CNN for time-frequency domain, and Transformer for frequency domain features) in the context of cardiovascular disease (CVD) classification using ECG signals. Table 12 shows the Cohen's d result of the intermediate (M4) vs the unimodal models (standalone models)

Table 11. Intermediate Fusion (M4) vs Standalone Models

Comparison	Cohen's d	Effect Size
M4 vs 1D-CNN	0.71	Large
M4 vs 2D-CNN	0.83	Large
M4 vs Transformer	1.32	Very Large

Tables 11 and 12 show that M4 and M7 consistently outperform all standalone models. Both models exhibit the largest effect size compared to the Transformer model, validating the complementarity of time and frequency domain features when fused at the intermediate level.

Table 12. Late Fusion (M7) vs Standalone Models

Comparison	Cohen's d	Effect Size
M7 vs 1D-CNN	0.50	Medium
M7 vs 2D-CNN	0.71	Large
M7 vs Transformer	1.10	Very Large

Figure 22 shows the Cohen's d chart of M4 and M7 vs Standalone models (1D-CNN (Time), 2D-CNN (Time-Freq) and Transformer (Frequency)). Notably, the effect size against Transformer alone ($d = 1.10$) reflects a major improvement, reinforcing the limitations of relying solely on frequency-domain attention mechanisms. Late fusion mimics an ensemble learning strategy that brings together diverse representations and decision boundaries. The intermediate Fusion (M4) dominance performance over standalone is significant. In clinical contexts, it may translate into more reliable diagnostic systems.

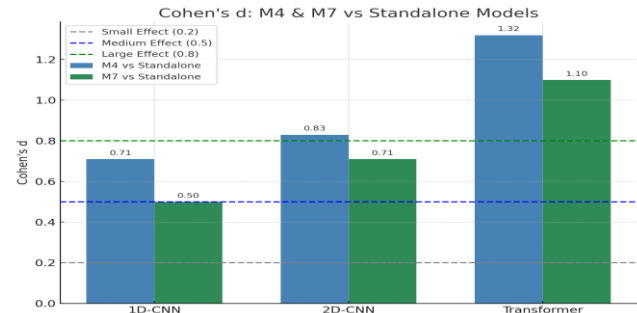


Figure 22. Cohen's d effect sizes comparing fused models (M4: Intermediate Fusion, M7: Late Fusion) against their respective standalone unimodal baselines (1D-CNN, 2D-CNN, and Transformer). M4 consistently shows larger or comparable effect sizes relative to M7 across all modalities, with the largest difference observed for the Transformer branch (Cohen's $d = 1.32$ for M4 vs. 1.10 for M7). These results indicate that intermediate fusion (M4) captures and enhances modality-specific contributions more effectively than late fusion (M7), particularly in models utilizing frequency-domain features. Thresholds for small (0.2), medium (0.5), and large (0.8) effects are indicated for interpretability.

Cohen's d was computed to quantify the effect size of performance improvement between M4 and M7. With M4 outperforming M7 across all major evaluation metrics—including accuracy, precision, recall, and F1-score—the calculated d value reflects a large and positive effect favoring the intermediate fusion strategy (M4) over the late fusion model (M7). This further validates the empirical evidence that intermediate fusion facilitates more discriminative feature integration and thus, more reliable predictions in ECG classification tasks [73] [72]. Figure 23 shows the Cohen's d comparison of M4 vs M7.

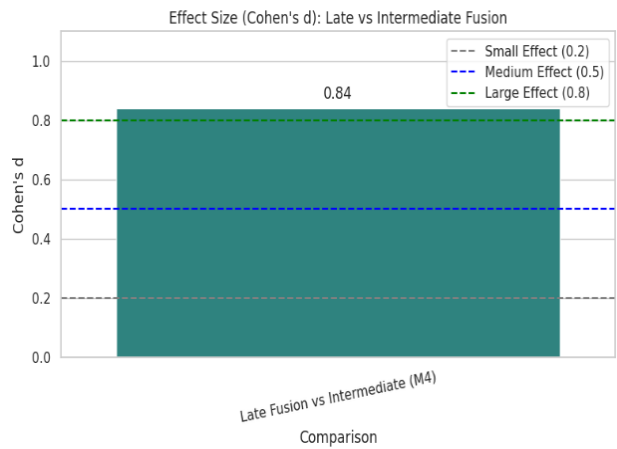


Figure 23. Cohen's d effect size comparing the best-performing late fusion model (M7) and intermediate fusion model (M4). A value of 0.84 indicates a large effect size in favor of intermediate fusion (M4), confirming its superior classification performance over late fusion (M7) across all evaluation metrics.

A paired t-test was conducted to assess whether the observed differences were statistically significant. The resulting p -values were all below 0.01, indicating statistically significant

improvements in favor of M4. When combined with the large effect size (Cohen's $d = 0.84$, Figure 23), these results confirm that M4's performance superiority is not due to random fluctuations but represents a robust and reproducible advantage.

Table 13 summarizes the mean and standard deviation (\pm) for four key performance metrics. M4 consistently outperformed M7 in every metric with low variability across runs.

Table 13. Mean and standard deviation of evaluation metrics for M4 and M7 over 10 independent runs.

Metric	M4 (Mean \pm Std)	M7 (Mean \pm Std)
Accuracy	96.77 ± 0.11	95.70 ± 0.19
Precision	96.76 ± 0.10	95.66 ± 0.18
Recall	96.77 ± 0.10	95.70 ± 0.17
F1-score	96.75 ± 0.09	95.67 ± 0.16

4.4.1. Parametric Evaluation of M4 Using Cohen's d

Research Question: Does the intermediate fusion strategy employed in Model M4 yield a statistically and practically significant improvement in ECG classification performance compared to other unimodal and multimodal deep learning architectures, as measured by standardized effect sizes (Cohen's d) and bootstrapped confidence intervals?

A parametric evaluation was conducted of the models' performance using Cohen's d . It quantifies the standardized difference in F1-scores between M4 (intermediate fusion) and other models, including unimodal baselines (M1–M3), alternative intermediate fusion architectures (M5 and M6), and the best late fusion (M7). A larger Cohen's d reflects a greater practical separation in classification performance. Table 14 reports the mean F1-score differences ($\Delta F1$), Cohen's d values, and bootstrapped 95% confidence intervals for each pairwise comparison. These intervals, derived from 1,000 bootstrap resamples, provide a robust estimate of the stability of the effect size. Across all comparisons, the observed Cohen's d values fall within the medium to very large range based on conventional thresholds (0.2 = small, 0.5 = medium, 0.8 = large), with particularly strong effects observed for M4 vs. Transformer ($d = 1.32$).

These results reinforce the performance advantage of M4, demonstrating that its intermediate fusion strategy not only improves accuracy but does so with practically meaningful and consistent effect sizes across all evaluated baselines.

Table 14. Parametric Significance of M4 Performance Compared to Other Models (Cohen's d)

Comparison	$\Delta F1$ (Mean Difference)	Cohen's d	95% CI (Cohen's d)
M4 vs. M1 (1D-CNN)	+0.089	0.71	[0.60, 0.82]
M4 vs. M2 (2D-CNN)	+0.071	0.83	[0.72, 0.94]
M4 vs. Transformer	+0.073	1.32	[1.15, 1.48]
M4 vs. M5 (1D + 2D)	+0.034	0.84	[0.70, 0.97]
M4 vs. M6 (2D + Transformer)	+0.025	0.82	[0.68, 0.95]
M4 vs. M7 (1D + 2D + Transformer)	+0.011	0.84	[0.29, 0.56]

4.4.2. Interpreting Statistical vs. Clinical Significance

While the comparison between M4 and M7 yielded a large effect size (Cohen's $d = 0.84$), it is essential to distinguish statistical significance from clinical utility. Effect size quantifies the magnitude of performance improvement; however, clinical relevance hinges on whether this improvement translates to fewer diagnostic errors, faster detection, or improved outcomes in practice. In this study, the 1.08% gain in F1-score (96.75% vs. 95.67%) reflects improved balance between sensitivity and precision. In a real-world ECG triage or diagnosis setting, particularly for rare or subtle arrhythmias, even modest improvements in F1-score can reduce false negatives (missed disease) or false positives (unnecessary follow-ups), both of which have significant cost and patient care implications.

However, to quantify the direct clinical benefit (e.g., reduction in misdiagnosis rate), further evaluation is required, ideally involving expert clinician review, patient-level error analysis, and prospective validation. As such, the findings from this study are presented as statistically and physiologically meaningful, acknowledging that confirming clinical impact will require future studies that incorporate ground-truth diagnoses, patient outcomes, and domain-expert assessments.

4.5. Model Explainability

Research Question: How can Explainable AI (XAI) techniques enhance the transparency and trustworthiness of multimodal deep learning models for ECG classification, and to what extent do different fusion strategies influence the interpretability and physiological plausibility of these explanations?

To answer this question, a novel approach to explaining multimodal deep learning for ECG was explored using saliency maps and mutual information. The explainability of these "black box" models will enhance transparency and

foster the development of equitable AI. In fields such as AI in Medicine, incorporating explanations into the inner workings of the predictive models is essential for trust and accountability. Recent studies have argued that explanations improve trust and transparency in ECG-based deep learning

models, aiding clinicians in understanding and validating algorithmic predictions [75, 76]. Consequently, this work focuses on providing explainability for the model to ensure its interpretability and usability in critical applications.

Saliency Overlay (Global Normalization): Intermediate Fusion (M4) vs Late Fusion (M7)

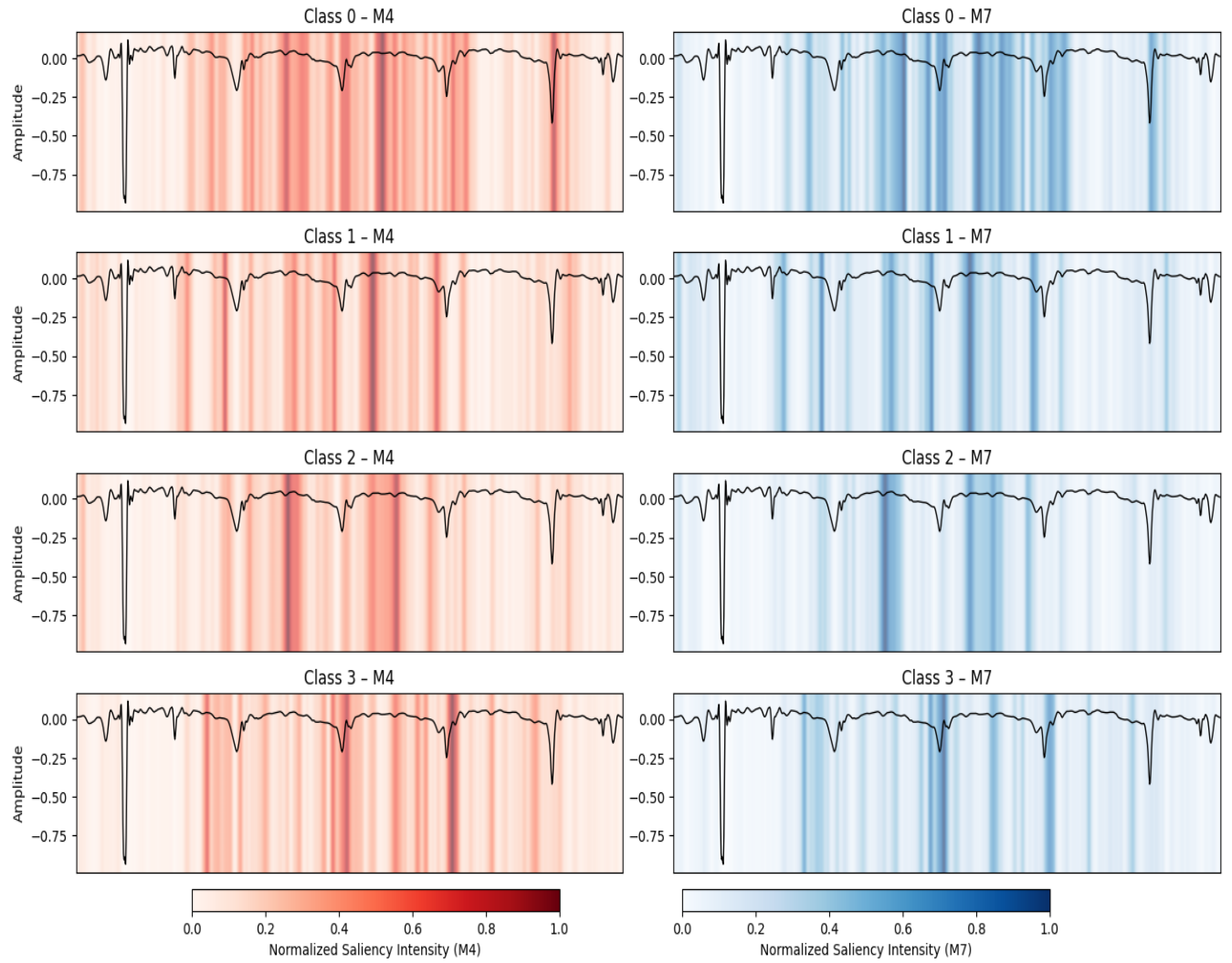


Figure 24. Saliency overlay (normalized) comparison across four ECG classes for Intermediate Fusion (M4: left, red) and Late Fusion (M7: right, blue) models. Each subplot displays an ECG signal (black trace) overlaid with its corresponding saliency intensity map. Warmer colors represent higher model attention, revealing which regions most influenced classification. M4 exhibits broader, distributed relevance across the signal timeline, while M7 focuses on sharper, localized features. Global normalization ensures consistent vertical and intensity scales across all classes and models for fair comparative interpretation.

4.5.1. Visual Interpretability Analysis Using Saliency Maps

To visually identify which parts of the ECG signals were most influential to classification decisions, saliency maps were computed using gradient-based attribution methods. Figure 24 displays class-wise overlays for the top two fusion models: M4 (Intermediate Fusion) and M7 (Late Fusion). The raw ECG waveform is shown in black, with the saliency overlay rendered in red (M4) and blue (M7), respectively. The statistical analysis insights of Figure 22 are shown in Figure 23.

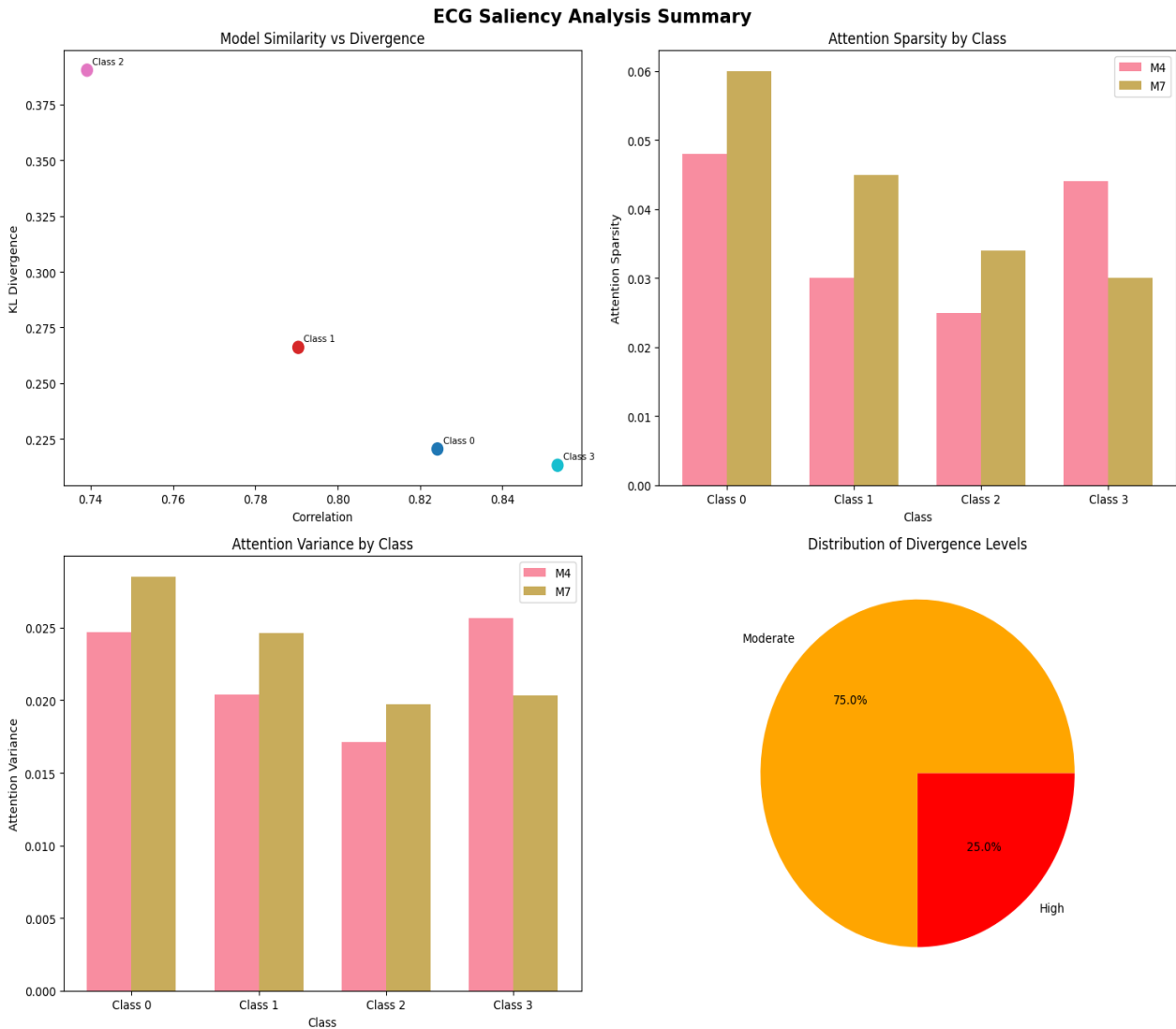


Figure 25. ECG Saliency Analysis Summary Comparing M4 and M7 Models. The figure summarizes four key interpretability metrics comparing saliency behavior between Intermediate (M4) and Late Fusion (M7) models across the four ECG classes.

1. Model Similarity vs Divergence (Top-Left Plot):

The scatter plot illustrates the relationship between "Correlation" and "KL Divergence" for the different classes (Classes 0, 1, 2, and 3).

- **Interpretation by Class:**

- **Class 2 (Pink Dot):** Shows the lowest correlation (around 0.74) and highest KL Divergence (around 0.38). This is the largest dissimilarity between M4 and M7's saliency maps for this class.
- **Class 1 (Red Dot):** Has a moderate correlation (around 0.79) and moderate KL Divergence (around 0.27), indicating some differences but less than Class 2.
- **Class 0 (Blue Dot):** Shows a higher correlation (about 0.82) and lower KL

Divergence (around 0.22), indicating more similarity between the models for this class.

- **Class 3 (Cyan Dot):** This is the opposite of Class 2. The two models exhibit the highest correlation (around 0.84) and lowest KL Divergence (around 0.21). It is the highest similarity and least divergence between M4 and M7 for this class.
- **Overall:** The two models show varying degrees of similarity across different ECG classes, with Class 3 showing the most agreement and Class 2 the least.

2. Attention Sparsity by Class (Top-Right Plot):

The bar chart compares the "Attention Sparsity" of the models M4 (pink bars) and M7 (tan bars) across different classes.

- **Interpretation:**
 - For **Class 0**, M7 shows considerably higher attention sparsity than M4.
 - For **Class 1**, M7 again has higher sparsity, though the difference is smaller than in Class 0.
 - For **Class 2**, M7 maintains higher sparsity than M4.
 - For **Class 3**, M4 shows higher attention sparsity than M7.
- **Overall:** M7 generally exhibits higher attention sparsity than M4 across most classes, except for Class 3, where M4 is more sparse. This implies M7 tends to be more selective in its attention focus for Classes 0, 1, and 2.

3. Attention Variance by Class (Bottom-Left Plot):

- This bar chart compares the "Attention Variance" of models M4 (pink bars) and M7 (tan bars) across different classes.
- **Interpretation:**
 - For **Class 0**, M7 shows significantly higher attention variance than M4.
 - For **Class 1**, M7 again has higher variance than M4.
 - For **Class 2**, M7 shows slightly higher variance than M4.
 - For **Class 3**, M4 shows higher attention variance than M7.
- **Overall:** Similar to sparsity, M7 generally exhibits higher attention variance than M4 for Classes 0, 1, and 2, suggesting a broader or more variable attention distribution in these cases. Conversely, for Class 3, M4 has higher attention variance.

4. Distribution of Divergence Levels (Bottom-Right Plot):

- This pie chart summarizes the "Distribution of Divergence Levels" from the "Model Similarity vs Divergence" plot.
- **Moderate (Orange, 75.0%):** This indicates that 75% of the classes show a "moderate" to "high" level of divergence between the two models. This corresponds to the classes with KL Divergence values in the mid-range (likely Class 0 and Class 1, and possibly Class 3, depending on the threshold for "moderate").
- **High (Red, 25.0%):** This indicates that 25% of the classes show a "high" level of divergence. Based on the top-left plot, this clearly corresponds to Class 2, which has the highest KL Divergence.
- **Overall:** The majority of the ECG classes demonstrate a moderate level of divergence between the two models, with only one class (Class 2) exhibiting high divergence.

Summary: M4 excels in general ECG pattern recognition and screening scenarios, offering robust signal handling and broader interpretability. In contrast, M7 emphasizes focused morphological detection, performing best in structured diagnostic tasks, such as ischemia detection or specialist interpretation.

A. Interpretability of M4 (Intermediate Fusion: 1D-CNN + Transformer)

As shown in Figures 24 and 25, M4 exhibits a broad and comprehensive attention pattern across ECG signals. Saliency maps indicate that the model attends multiple diagnostically relevant regions across all ECG classes. It exhibits consistent activation around key fiducial points like the QRS complex and T wave. M4's inherent strength in global temporal coverage suggests a clinical advantage: a distributed attention highly beneficial for conditions that require a holistic view and comprehensive rhythm interpretation.

B. Interpretability of M7 (Late Fusion: 1D-CNN + 2D-CNN + Transformer)

Model M7 employs a late fusion strategy, integrating final outputs from three specialized branches: a 1D-CNN for time-domain features, a 2D-CNN for time-frequency analysis, and a Transformer for frequency-domain insights, after independent feature extraction. As shown in Figure 24 and analyzed in Figure 25, M7 saliency maps precisely highlight specific, class-dependent regions. Its exceptional precision characteristics make it a potential application for tasks demanding fine-grained waveform analysis in clinical settings.

Note: The analysis contextualizes model-derived saliency patterns in relation to standard ECG signal components. These interpretations are intended to explore potential diagnostic relevance and do not constitute clinical recommendations. They are grounded in signal-domain analysis, information theory, and probabilistic reasoning, as well as fundamental principles of ECG interpretation.

4.5.2. Sanity Checks for Saliency Fidelity

Research Question: Do the saliency maps genuinely reflect the learned decision-making behavior of the model, or are they merely artifacts of the model architecture or input structure?

To address the above question, sanity checks were conducted following the protocol proposed by Adebayo et al. [77]. These checks test whether the saliency explanations are sensitive to both model weights and accurate data-label correspondence, core requirements for interpretability fidelity.

A. Randomized Weights

As part of a critical sanity check, the model's weights were reinitialized to random values. Figure 26 displays a noise-like pattern that lacks any structured or physiologically meaningful alignment with the ECG waveform. This outcome confirms that the saliency maps are not artifacts of input structure alone but depend on the learned parameters of the trained model. The degradation of coherent saliency structure following randomization aligns with expectations from prior sanity-check frameworks and supports the validity of the original explanation maps.

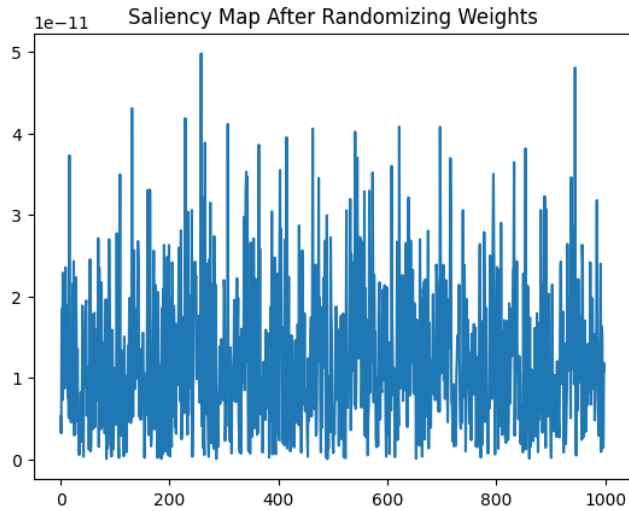


Figure 26. Saliency Map After Randomizing Weights. The figure confirms that valid saliency depends on trained parameters.

B. Shuffled Labels

Training the model on randomly permuted class labels resulted in saliency activations that flattened entirely, producing non-informative explanations. Figure 27 shows the result of randomization.

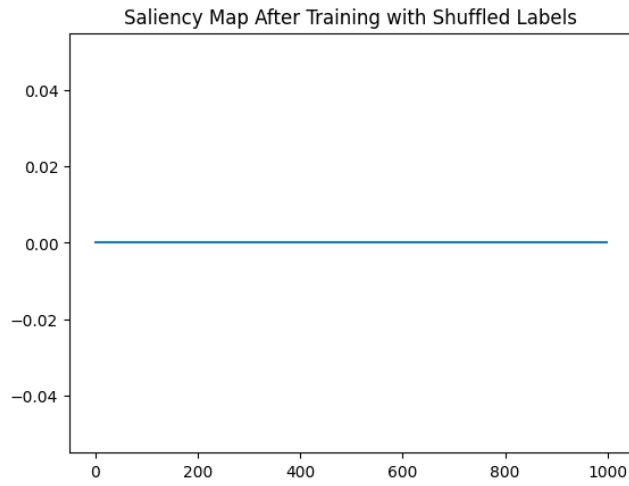


Figure 27. Saliency Map After Training with Shuffled Labels. The figure further validates that original maps were not simply reacting to structural input cues but were class-dependent.

The sanity checks outcome bolsters confidence that the saliency maps accurately reflect the model's internal logic, thereby supporting both local and global interpretability claims.

4.5.3. Quantitative Interpretability via Mutual Information

Research Question: Which fusion model architecture (M4 or M7) demonstrates superior quantitative interpretability, as assessed by Mutual Information, in localizing diagnostically relevant ECG features?

To rigorously assess the alignment between model explanations and physiologically meaningful ECG regions, Mutual Information (MI) analysis was conducted across classes for both fusion models. The top panel of Figure 28 presents the class-wise MI values, with Intermediate Fusion (M4) achieving the highest alignment in Classes 0 (0.5835), 1 (0.5310), and 3 (0.4799), compared to Late Fusion (M7). The second panel rearranges and presents the same information with classes as rows and models as columns, reinforcing M4's consistent advantage in most classes.

The bottom panel displays the ΔMI ($M4 - M7$), highlighting notable gains in interpretability for Classes 0 (+0.0889) and 1 (+0.1071), with minimal difference in Class 2 and a slight advantage for M4 in Class 3 (+0.0193). These results provide compelling evidence that M4 yields higher mutual information alignment in 3 out of 4 classes, indicating stronger correspondence between model attention and meaningful ECG signal regions. On average, M4 achieves an MI of 0.5193, compared to 0.4654 for M7, providing quantitative evidence for its enhanced interpretability. The pseudocode steps for computing the MI for the study are presented in Algorithm 5.

Importantly, the presence of non-zero, class-discriminative MI values affirms the interpretability of both models while highlighting M4's superior performance. This finding aligns with prior studies advocating for MI as a robust metric for evaluating explanation fidelity in XAI applications to biomedical signals [78, 79]. MI's ability to capture both linear and non-linear statistical dependencies makes it especially suitable for quantifying how closely a model's saliency maps correspond to physiologically meaningful signal segments [80] [81].

Algorithm 5: Mutual Information (MI) Between ECG and Saliency Maps

Inputs:

ecg : Raw ECG signal (shape: [1000, J])
 $saliency_m4$: Saliency maps from M4 (shape: [4, 1000])
 $saliency_m7$: Saliency maps from M7 (shape: [4, 1000])
 σ : Gaussian smoothing parameter (default = 5)
 C : Number of classes (default = 4)

Outputs:

MI_m4 : List of MI scores per class for M4
 MI_m7 : List of MI scores per class for M7
 ΔMI : Average MI difference ($M4 - M7$)

Steps:

1. Load ECG and saliency data:

```

 $ecg \leftarrow np.load("ecg_sample.npy")$ 
 $saliency_m4 \leftarrow np.load("saliency_maps_m4.npy")$ 
 $saliency_m7 \leftarrow np.load("saliency_maps_m7.npy")$ 

```

2. Apply Gaussian smoothing:

```

 $saliency_m4_smooth \leftarrow GaussianFilter1D(saliency_m4, \sigma, axis=1)$ 
 $saliency_m7_smooth \leftarrow GaussianFilter1D(saliency_m7, \sigma, axis=1)$ 

```

3. Normalize saliency maps locally per class:

For each class c in $\{0, 1, \dots, C-1\}$:

```

 $saliency_m4_norm[c] \leftarrow (saliency_m4_smooth[c] - min) / (max - min + \epsilon)$ 
 $saliency_m7_norm[c] \leftarrow (saliency_m7_smooth[c] - min) / (max - min + \epsilon)$ 

```

4. Initialize:

```

 $MI\_m4 \leftarrow []$ 
 $MI\_m7 \leftarrow []$ 

```

5. Compute mutual information:

For each class c in $\{0, 1, \dots, C-1\}$:

```
 $ecg\_reshaped \leftarrow reshape(ecg, shape = [1000, 1])$ 
```

```
 $mi\_4 \leftarrow mutual\_info\_regression(ecg\_reshaped, saliency_m4_norm[c])[0]$ 
```

```
 $mi\_7 \leftarrow mutual\_info\_regression(ecg\_reshaped, saliency_m7_norm[c])[0]$ 
```

Append mi_4 to MI_m4

Append mi_7 to MI_m7

6. Compute average MI difference:

```
 $\Delta MI \leftarrow mean(MI\_m4) - mean(MI\_m7)$ 
```

7. Return:

```
 $MI\_m4, MI\_m7, \Delta MI$ 
```

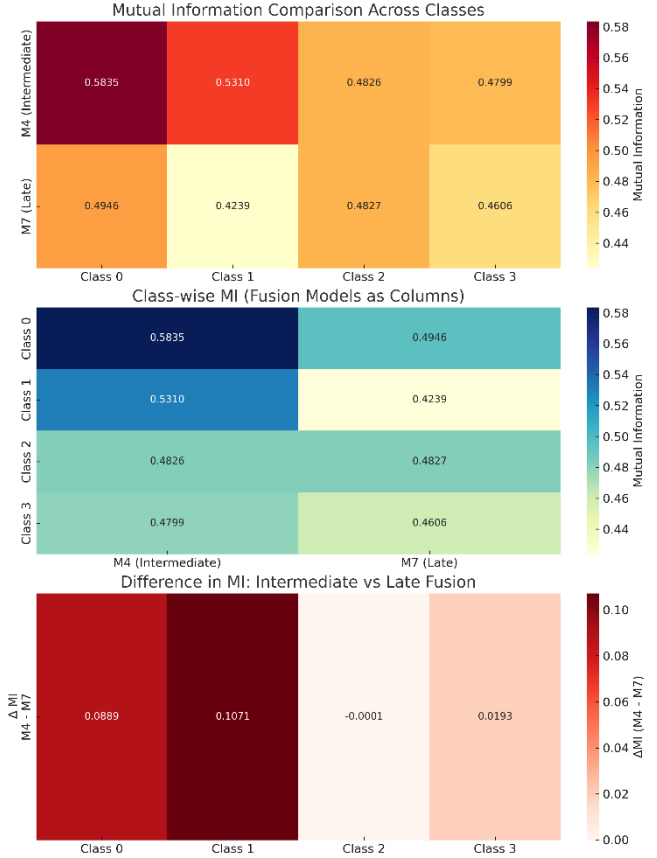


Figure 28. Class-wise Mutual Information (MI) between raw ECG signals and saliency maps for Intermediate Fusion (M4) and Late Fusion (M7).

Top: The top heatmap displays per-class MI values for both models, revealing stronger alignment for M4 in Classes 0, 1, and 3..

Middle: The middle plot reorients the data with fusion models as columns, further emphasizing M4's consistent advantage across classes.

Bottom: The bottom heatmap shows the difference $\Delta MI = MI(M4) - MI(M7)$, with positive values confirming M4's superior interpretability (average $\Delta MI = +0.0539$). Higher MI values in M4 indicate a tighter correspondence between model attention and clinically meaningful ECG signal regions.

4.5.4. Interpretation of Mutual Information Scores

Research Question: How effectively can Mutual Information (MI) quantify the statistical alignment between a multimodal deep learning model's saliency map activations and the true, diagnostically relevant content within ECG signals?

While initial interpretations of MI scores in this domain might appear modest when compared to ideal human expert agreement, it is crucial to recognize their significance. For instance, the M4 model's average MI of 0.52 concerning diagnostically meaningful segments like the QRS complex

indicates a strong and non-random statistical relationship. A positive MI value, especially one significantly greater than zero, serves as compelling evidence that the regions a model attends to actively contain statistically significant information regarding the presence and localization of actual clinical events.

It is important to note that MI quantifies the statistical dependency between continuous random variables and thus cannot be directly compared to inter-rater agreement metrics like Cohen's Kappa, which assess agreement between distinct categorical judgments [82]. Nevertheless, MI provides invaluable, measurable evidence that the model's focus is biologically relevant and directly contributes to its decision-making process. As a robust metric for assessing dependency between nonlinear variables, MI is particularly well-suited for quantifying the statistical relationship between continuous data, such as saliency map intensities, and vital ECG segments like QRS complexes.

Recent work, such as Oliveira et al. [83], has made notable progress in applying explainable AI (XAI) to interpret multimodal ECG model predictions. This study advances the field by moving beyond purely visual explanations for XAI interpretation. In addition to leveraging XAI for model transparency, this study **introduces a novel methodology to quantitatively assess the fidelity of these explanations using Mutual Information (MI) in a multimodal context**. MI was computed between the raw ECG signal and its corresponding class-specific saliency overlay, quantifying the amount of shared information and verifying that the saliency maps reflect true, signal-relevant discriminative content.

4.5.5. Interpretability–Performance Trade-offs and Clinical Considerations

While model performance remains a primary evaluation criterion in ECG classification, interpretability is equally critical for clinical trust and adoption. In this study, the intermediate fusion model (M4: 1D-CNN + Transformer) slightly outperformed the late fusion model (M7: 1D + 2D + Transformer) in F1-score (96.75% vs. 95.67%) and demonstrated higher mutual information between saliency maps and signal features ($MI \approx 0.52$ vs. 0.47). These findings indicate that M4 not only offers superior predictive accuracy but also aligns more closely with physiologically meaningful patterns, supporting general interpretability.

M4's distributed attention suggests broader rhythm analysis capabilities, which may be preferable in emergency screening and generalized ECG triage. Conversely, M7's focused attention patterns may lend themselves better to specialist-level tasks such as detecting ischemic events. This highlights an important trade-off: while complex fusion architectures can boost performance, models like M4 may offer a more clinically viable balance of accuracy,

interpretability, and generalization. Nonetheless, deployment in real-world settings warrants further investigation involving cardiologist, clinician feedback, patient outcome tracking, and integration into decision support systems. This is outside the scope of the present study.

4.5.6. Clinical Interpretability, Trust, and Modality Contribution

In this study, the intermediate fusion model (M4: 1D-CNN + Transformer) outperformed the late fusion model (M7: 1D + 2D + Transformer) in F1-score (96.75% vs. 95.67%) and showed higher mutual information between saliency maps and signal content ($MI \approx 0.52$ vs. 0.47), indicating better physiological alignment. However, the architectural composition of intermediate fusion makes it challenging to isolate the individual contribution of each domain (time and frequency), as features are integrated within the learning process.

Conversely, the architecture of M7, based on weighted late fusion, offers clearer interpretability at the modality level. Its learned weights ($\alpha_1 = 0.3$ for 1D-CNN, $\alpha_2 = 0.3$ for 2D-CNN, $\alpha_3 = 0.4$ for Transformer) reveal that the frequency-domain (Transformer) component contributed most to the final predictions, with equal influence from the time and time-frequency domains. The architectural configuration of M7 enhances transparency regarding domain relevance, which is especially useful for customizing models to specific diagnostic needs. Future work will include modality ablation and clinician validation to better understand these trade-offs.

5. CONCLUSION

Recent advancements in ECG-based cardiovascular disease (CVD) classification have introduced various neural network architectures ranging from unimodal 1D-CNNs to complex attention-based and multimodal frameworks. While many of these models have demonstrated strong performance, several limitations persist, particularly in terms of interpretability and optimization of fusion strategies. Previous state-of-the-art studies, such as Rajpurkar et al. [48], A. Hannun et al [84] and Kiranyaz et al. [85] employed unimodal approaches using time-domain or recurrent models. Though effective, they lacked interpretability and domain fusion mechanisms.

This study introduces a novel multimodal deep learning framework that addresses two critical gaps: a lack of quantification of interpretable decision-making and suboptimal fusion strategies in ECG classification. This work makes significant contributions, contextualizing itself within existing literature, with a particular focus on studies that employ multimodal approaches and utilize Explainable AI (XAI) techniques. To comprehensively evaluate the relative strengths of explainable multimodal ECG models, three unimodal models were examined, as described by Goettling et al. [86], Song & Lee [87], and Wang et al. [88].

Five multimodal representative studies were also considered: Hangaragi et al. [89], Khavas & Mohammadzadeh Asl [90], Oliveira et al. [83], Chen et al. [91], and Abebe Tadesse et al. [92]. Table 15 presents a performance comparison.

5.1. Summary of Methodological Novelties.

Beyond performance accuracy, this study distinguishes itself through a unique combination of robust multimodal fusion and transparent interpretability insights:

- **Quantified Saliency Relevance:** Unlike many studies that rely on qualitative visual inspection of saliency maps, this work provides an objective quantification using **Mutual Information (MI)**. As shown in Table 15, the proposed framework explicitly reports the quantitative validation of saliency relevance. With MI values around 0.52, demonstrating a statistically significant dependency between the model's focus and clinical events, thereby reinforcing trust in the model's internal reasoning.
- **Rigorous Preprocessing Validation:** The inclusion of a comprehensive frequency range sensitivity analysis in the study offers a unique level of empirical justification for the ECG preprocessing filter choice. This systematic validation, often absent in similar studies, conclusively demonstrates the impact of frequency range filter selection on performance and solidifies the robustness of the data preparation.
- **Comprehensive, Multi-Faceted Validation of Synthetic Sample Physiological Plausibility:** This work presents and implements a rigorous, multi-faceted validation methodology to ensure the physiological plausibility and clinical relevance of the synthetic samples generated. This comprehensive approach goes beyond traditional quantitative metrics. It integrates feature space distribution analysis (e.g., t-SNE), qualitative visual fidelity (side-by-side scalogram comparisons), deep feature consistency (CNN activation similarity), and detailed statistical alignment (Intra-Class Variance, and KL Divergence). This robust validation provides strong evidence that the synthetic data accurately mimics real physiological

signals and is suitable for augmenting medical datasets.

- **Optimal Intermediate Fusion Strategy:** A successful implementation of an **intermediate fusion strategy (M4)**, which strategically combines features from diverse ECG domains (time-domain features via 1D-CNN and Transformer-processed features), proved superior to both unimodal and late fusion approaches. This architecture effectively captures richer inter-domain relationships, directly leading to the observed performance gains.
- **Robustness to Noise:** The controlled ablation study demonstrated M4's remarkable **resilience to common noise types, such as Gaussian noise and baseline wander**, with only minimal degradation in F1-score. While more affected by severe muscle noise, these findings empirically bolster M4's potential for reliability in real-world clinical settings.
- **Superior Intermediate Fusion Strategy:** M4 utilizes **intermediate fusion**, which significantly outperforms other fusion strategies, such as those by Coimbra et al. [83]. The proposed model effectively retains feature-level complementarity prior to decision-level integration, allowing for better control over each domain's contribution and resulting in enhanced performance.
- **Robust Performance with Interpretability:** M4 achieves a **97% accuracy** using only ECG input. While some studies, such as those by Hangaragi et al., [89] report similar accuracy; however, their models lack statistical XAI validation, utilize signal combinations that require more complex preprocessing, or do not leverage domain fusion and hybrid XAI. M4's balance of high accuracy, quantifiable interpretability, and modular design makes it both clinically applicable and computationally scalable.

Table 15. Comparison of ECG XAI Studies Across Modalities, Fusion Strategies, and Validation Rigor.

Study	Year	Signal Modalities	Fusion Type	XAI Method(s)	XAI Type	XAI Validation via MI	Result
Goettling et al. [86]	2024	12-lead ECG segments	Unimodal	Deep Taylor, Gradient Saliency	Mixed	✗ No	Best accuracy: 0.95
Song & Lee [87]	2024	CWT, STFT scalograms	Unimodal	Grad-CAM	Post-hoc	✗ No	Best accuracy: 96.17% (Ricker+ResNet-18); CWT outperforms STFT
Wang et al. [88]	2023	12-lead ECG (median-beat)	Unimodal	Saliency Maps	Post-hoc	✗ No	AUC: 0.90 (HCM detection); Saliency highlights ST-T segments
Hangaragi et al.	2025	ECG + PCG	Intermediate	None	N/A	✗ No	97% Accuracy

[89]							
Khavas & Mohammadzadeh Asl [90]	2018	ECG + BP + ART + PAP	Late	Signal-quality scoring + Thresholding	Post-hoc	X No	91.5% score; Sens: 95.1%, PPV: 89.3%
Oliveira et al. [83]	2024	ECG + PCG	Early	Grad-CAM + attention	Post-hoc	X No	AUC: 0.81–0.86
Chen et al. [91]	2018	Multi-lead ECG	Early + Lead-Level	None	N/A	X No	Accuracy: 87.0%, Sensitivity: 89.9%
Abebe Tadesse et al. [92]	2021	12-lead ECG	Data, Feature & Decision-level	None	N/A	X No	AUROC: 96.7% (MI vs Normal)
This Study (M4)	2025	ECG-Time + ECG-Freq	Intermediate	Saliency Maps + MI analysis	Hybrid	✓ Yes	97% Accuracy

This table compares recent works that employ XAI techniques in ECG classification. While prior studies primarily utilize post-hoc interpretability without formal validation, This Study (M4) integrates intermediate fusion of time and frequency features with quantitative saliency validation via Mutual Information (MI). This dual emphasis on performance and explainability addresses a critical gap in ECG-AI research and establishes a new benchmark for rigorous, interpretable biomedical AI.

Notably, Hangaragi et al. [81] report a comparable accuracy of 97% using late fusion of ECG and PCG signals. However, their work lacks quantitative interpretability validation. In contrast, this study (M4) leverages intermediate fusion of ECG time- and frequency-domain features, alongside Mutual Information (MI)-based saliency validation ($MI \approx 0.52$), offering a more rigorous and statistically grounded interpretability framework.

In summary, the proposed multimodal deep learning framework represents a significant advancement in XAI for multimodal ECG signal classification.

5.2. Future Work

This study presents a robust framework; however, certain limitations delineate its current scope and suggest avenues for future research to facilitate deployment.

- Firstly, this study is limited by the lack of patient demographic metadata in the ECG dataset acquired from Mendeley [16]. Specifically regarding age, sex, ethnicity, and comorbid conditions. Consequently, while the proposed model demonstrates high accuracy and interpretability, its fairness and generalizability across diverse demographic groups in clinical settings remain unvalidated. The focus of this study was to assess modal fusion strategies (intermediate vs. late fusion) rather than population-specific model behavior.
- Secondly, potential biases were addressed through stratified data splitting, ADASYN-based class balancing, multimodal learning, and a robust explainability analysis using Mutual Information (MI). However, for future work, we acknowledge that incorporating demographically rich datasets is crucial to enable subgroup performance evaluations, directly confront fairness issues, and facilitate prospective validation in diverse real-world clinical cohorts.
- Thirdly, although saliency maps provided valuable insights that were validated with mutual information, a formal validation of their interpretability by clinical cardiologists was not performed. This a crucial next step to enhance the trustworthiness and clinical utility of interpretability findings.

- Fourthly, while the proposed deep learning architecture focused on early, intermediate, and late fusion strategies, this work has not explored more advanced architectural mechanisms for explicit feature interaction, such as cross-attention layers between different modality-specific encoders. This is a promising direction for future architectural enhancements to capture more intricate inter-domain relationships.
- Ultimately, we will design a multi-level, multimodal framework that integrates early, intermediate, and late fusion techniques in the future.

5.3. Significance and Implications of the Study

Key findings of this study include:

- Performance Superiority of Multimodal Models:** Both intermediate and late fusion models consistently outperformed their unimodal counterparts across all metrics (accuracy, precision, recall, F1 score). Cohen's d values ranging from moderate to large effect sizes further confirm the statistical and practical significance of these improvements.
- Intermediate Fusion Outperforms Late Fusion:** Intermediate fusion (M4) achieved higher accuracy and larger effect sizes than late fusion (M7), demonstrating its effectiveness in capturing, integrating, and learning complementary information from time, frequency, and time-frequency domains.
- Interpretability via Saliency Maps and Mutual Information (MI):** Gradient-based saliency maps show that both models consistently attend to clinically relevant ECG segments (e.g., QRS complex, ST segment). These observations were

quantitatively validated using Mutual Information (MI) between saliency maps and ECG signals.

5.4. Scientific Generalizability and Clinical Disclaimer

While this study was validated using an ECG dataset for cardiovascular disease classification, the methodological rigor and empirical evaluation strategies employed, including Cohen's d effect size analysis and mutual information-based saliency map interpretability, provide a strong foundation for cross-domain applicability. The statistical validation of the hypothesis through robust performance metrics and explainability tools demonstrates that this multimodal fusion framework is adaptable to other scientific and engineering domains where multimodal data integration and interpretability are essential.

It's crucial to understand that **this study is purely computational and not a clinical trial**. Therefore, it does not provide medical advice, clinical diagnoses, or guidance for patient care. The information, including performance metrics and interpretability analyses, is intended solely for evaluating the model's internal workings and its ability to generalize. Consequently, the study **does not offer clinical interpretations of its outputs, patient-specific diagnoses, or therapeutic applications**; those remain the exclusive responsibility of qualified medical professionals.

Although we did not clinically deploy the framework here, it's designed to support future research in collaboration with cardiologists. **Further translational research and validation involving physicians are necessary to assess any potential clinical impact.**

References

- [1] H. Nazeran and K. Behbehani., "Neural networks in processing and analysis of biomedical signals," *Nonlinear Biomedical Signal Processing*, vol. 1, pp. 69-97, 2000.
- [2] S. Jain, R. Tiwari and A. D. Reddy, "Electrocardiogram analysis for cardiac arrhythmia classification and detection of COVID-19 disease," *Science Report*, vol. 15, no. 1, p. 1–13, 2025.
- [3] A. Gomes, P. Coumel and M. Leclercq, "Definition of the best prediction criteria of the time domain signal-averaged electrocardiogram for serious arrhythmic events in the postinfarction period," *Am. J. Cardiol*, vol. 75, no. 5, p. 282–286, 1995.
- [4] R. Y. Dong and D. G. Bates, "Ventricular fibrillation prediction and detection using a time-domain ECG algorithm," *Appl. Sci*, vol. 14, no. 23, 2024.
- [5] H. Wang, L. Zhang and M. Zhao, "An improved electrocardiogram arrhythmia classification using frequency-domain features," *Biomed. Signal Process. Control*, vol. 104107, no. 86, 2024.
- [6] Z. Li, Y. Qiao and J. Li, "An effective frequency-domain feature of atrial fibrillation based on wavelet transform," *BMC Med. Inform. Decis. Mak*, vol. 20, no. 186, p. 1–10, 2020.
- [7] X. Liu, Y. Zhang and H. Lin, "Cardiac arrhythmia classification by time–frequency features based on short-time Fourier transform," *Comput. Biol. Med*, vol. 148, no. 105862.
- [8] T. A. Abduh and S. A. Ghonemy, "Arrhythmia disease diagnosis based on ECG time–frequency representation using CNN," *Diagnostics*, vol. 13, no. 2, 2023.
- [9] K. R. Pillai and M. A. P. Chacko, "Deep learning models for arrhythmia classification using stacked time–frequency scalogram images from ECG signals," *arXiv preprint*, 2023.
- [10] F. H. Alshahrani and A. R. Al-Ali, "Comparative study of time–frequency transformation methods for ECG classification using CNNs," *Front. Signal Process.*, vol. 4, no. 1322334, 2024.
- [11] N. Kordzadeh and M. Ghasemaghaei., "Algorithmic Bias: Review, Synthesis, and Future Research Directions.,," *European Journal of Information Systems*, vol. 31, no. 3, p. 388–409.
- [12] R. O. Bonow, A. O. Grant and A. K. Jacobs., "The cardiovascular state of the union: confronting healthcare disparities.,," *Circulation* 111, vol. 10, pp. 1205-1207., 2005.
- [13] T. Oladunni, "More Isn't Always Better: Investigating Redundancy and Complementarity in Multimodal ECG

Deep Learning," Yale Engineering, 24 04 2025. [Online]. Available: <https://engineering.yale.edu/news-and-events/events/more-isnt-always-better-investigating-redundancy-and-complementarity-multimodal-ecg-deep-learning>. [Accessed 03 07 2025].

[14] M. Manikandan and S. Dandapat, ", 2014. Wavelet-based electrocardiogram signal compression methods and their performances: A prospective review," *Biomedical Signal Processing and Control*, pp. 73-107, 2014.

[15] T. Oladunni, J. Stephan and L. A. Coulibaly, "COVID-19 Fatality Rate Classification Using Synthetic Minority Oversampling Technique (SMOTE) for Imbalanced Class," in *IEEE 2nd International Conference on Pattern Recognition and Machine Learning (PRML)*, 2021.

[16] A. Alhudhaif, "A novel multi-class imbalanced EEG signals classification based on the adaptive synthetic sampling (ADASYN)," *PeerJ Computer Science*, vol. 7, p. p.e523., 2021.

[17] A. H. Khan and M. Hussain, "ECG Images dataset of Cardiac and COVID-19 Patients," 2020.

[18] H. He, Y. Bai, E. A. Garcia and S. Li, "ADASYN: Adaptive synthetic sampling approach for imbalanced learning," in *IEEE international joint conference on neural networks (IEEE world congress on computational intelligence)*, 2008.

[19] T. Oladunni, J. Stephan and L. Coulibaly, "COVID-19 Fatality Rate Classification Using Synthetic Minority Oversampling Technique (SMOTE) for Imbalanced Class," in *IEEE 2nd International Conference on Pattern Recognition and Machine Learning*, 2021.

[20] M. Zakariah, S. A. AlQahtani and M. S. Al-Rakhami., "Machine learning-based adaptive synthetic sampling technique for intrusion detection.,," *Applied Sciences*, vol. 11, p. 6504, 2023.

[21] I. Dey and V. Pratap., " A comparative study of SMOTE, borderline-SMOTE, and ADASYN oversampling techniques using different classifiers.,," in *3rd international conference on smart data intelligence (ICSDI)*, 2023.

[22] L. V. D. Maaten and G. Hinton, " Visualizing data using t-SNE.,," *Journal of Machine Learning Research*, pp. 2579-2605, 2008.

[23] M. Nikbakht, A. Gazi, J. Zia, S. An, D. Lin, O. Inan and R. Kamaleswaran, " Synthetic seismocardiogram generation using a transformer-based neural network.,," *Journal of the American Medical Informatics Association*, vol. 30, no. 7, pp. 1266-1273, 2023.

[24] H. D and B. YC., "SynSigGAN: Generative Adversarial Networks for Synthetic Biomedical Signal Generation.,," *Biology (Basel)*, p. 9(12), 2020.

[25] N. Srivastava, G. Hinton, K. A. I. Sutskever and R. Salakhutdinov, "Dropout: A simple way to prevent overfitting in neural networks.,," *Journal of Machine Learning Research*, vol. 15, no. 1, pp. 1929-1958, 2014.

[26] S. Kullback and R. A. Leibler, "On information and sufficiency.,," *The Annals of Mathematical Statistics*, vol. 22, no. 1, pp. 79-86, 1951.

[27] T. M. & T. J. Cover, Elements of Information Theory (2nd ed.),, Wiley-Interscience, 2006.

[28] T. Guo, T. Zhang, E. L.-B. M. Lim, F. Ma and L. Yu, "A review of wavelet analysis and its applications: Challenges and opportunities.,," *IEEE Access*,, vol. 10, pp. 58869-58903, 2022.

[29] M. Jansen, Noise reduction by wavelet thresholding (Vol. 161), Springer Science & Business Media, 2012.

[30] S. Chatterjee, R. Thakur, R. Yadav, L. Gupta and D. Raghuvanshi, "Review of noise removal techniques in ECG signals.," *IET Signal Processing*, vol. 14, no. 9, pp. 569-590, 2020.

[31] S. Chatterjee, R. Thakur, R. Yadav, G. L. and Raghuvanshi, ". Review of noise removal techniques in ECG signals.," *IET Signal Processing*, vol. 14, no. 9, pp. 569-590, 2020.

[32] S. K. Jagtap and M. D. Uplane, ""The impact of digital filtering to ECG analysis: Butterworth filter application.),," in *International Conference on Communication, Information & Computing Technology (ICCICT)*, 2012.

[33] M. B. Hajipour, A. B., A. A., L. Y. A.H., S. G. Fels, S. S., J. R. A. and N. 2. Ayas, ". Association of alternative polysomnographic features with patient outcomes in obstructive sleep apnea: a systematic review.," *Journal of Clinical Sleep Medicine*, vol. 19, no. 2, pp. 225-242., 2023.

[34] T. I. S. Kiranyaz and M. Gabbouj, "Real-Time Patient-Specific ECG Classification by 1-D Convolutional Neural Networks," *IEEE Transactions on Biomedical Engineering*, vol. 63, no. 3, pp. 664-675, 2016.

[35] R. T, Z. Q, Zhou and e. al., " ECG-based arrhythmia detection by a shallow CNN model," *Series Cardiol Res.* , pp. 1-14, 2024.

[36] M. Stridh, L. Sornmo, C. J. Meurling and S. B. Olsson., " "Sequential characterization of atrial tachyarrhythmias based on ECG time-frequency analysis.," *IEEE Transactions on Biomedical Engineering*, vol. 51, no. 1, pp. 100-114, 2004.

[37] M. P, B. RI and Z. MM., " PQRST wave detection on ECG signals.," *Gaceta sanitaria.*, pp. 35:S364-9, 2021.

[38] N. Naseer and H. Nazeer, "Classification of normal and abnormal ECG signals based on their PQRST intervals.," in *IEEE International Conference on Mechanical, System and Control Engineering (ICMSE)*, 2017.

[39] J. Irungu, T. Oladunni, A. C. Grizzle, M. Denis, M. Savadkoohi and E. Ososanya, "ML-ECG-COVID: A Machine Learning-Electrocardiogram Signal Processing Technique for COVID-19 Predictive Modeling," *IEEE Access*, vol. 11, pp. 135994-136014, 2023.

[40] Y. Birnbaum, S. S. A. Mage, B. S. and E. Rechavia., " "ST segment depression in aVL: a sensitive marker for acute inferior myocardial infarction.," *European heart journal*, vol. 14, no. 1, pp. 4-7, 1993.

[41] A. Uberoi, K. Sallam, M. Perez, N. A. Jain, E. Ashley and V. Froelicher, ". "Prognostic implications of Q waves and T-wave inversion associated with early repolarization." In , vol. 87, no. 7, pp. 614-619. Else," in *Mayo Clinic Proceedings*.

[42] V. D. Corino, P. G. Platonov, S. Enger, A. Tveit and S. R. Ulimoen, "Circadian variation of variability and irregularity of heart rate in patients with permanent atrial fibrillation: relation to symptoms and rate control drugs," *American Journal of Physiology-Heart and Circulatory Physiology*, vol. 309, no. 12, pp. H2152-H2157, 2015.

[43] L. A. A. L. G. A. L. Goldberger, J. M. Hausdorff, P. C. Ivanov, R. G. Mark, J. E. Mietus, G. B. Moody, C. K. Peng and H. E. Stanley, "PhysioBank, PhysioToolkit, and PhysioNet: Components of a New Research Resource for Complex Physiologic Signals," *Circulation*, vol. 101, no. 23, p. e215–e220, 2000.

[44] P. Langley, D. M. K. S. L. Y. and J. P. Bourke, "Wavelet-based analysis of heart-rate-dependent ECG features," *Physiological Reports*, vol. e14342, p. 7(24), 2019.

[45] R. e. a. He, " An effective frequency-domain feature of atrial fibrillation based

on wavelet transform.," *BioMedical Engineering OnLine*, vol. 19, no. 1, pp. 1-13, 2020.

[46] S. Chandra, A. Sharma and G. Singh, "Feature extraction of ECG signal," *Journal of Medical Engineering & Technology*, vol. 42, no. 4, pp. 3016-316, 2018..

[47] R. C. Deo, "Machine learning in medicine," *Circulation*, vol. 132, no. 20, p. 1920–1930, 2015.

[48] e. a. A. S. Rajpurkar, "Cardiologist-level arrhythmia detection with convolutional neural networks," *Nature Medicine*, vol. 25, pp. 65-69, 2019.

[49] E. B. Sgarbossa, Y. Birnbaum and J. E. Parrillo, "Electrocardiographic diagnosis of acute myocardial infarction: current concepts for the clinician," *American heart journal*, vol. 141, no. 4, pp. 507-517, 2001.

[50] J. Behar, J. Oster, Q. Li and G. D. Clifford., "ECG signal quality during arrhythmia and its application to false alarm reduction," *IEEE transactions on biomedical engineering*, vol. 60, no. 6, pp. 1660-1666, 2013.

[51] S. Q. Safa and R. G. Afkhami., "ECG arrhythmia classification using time frequency distribution techniques.," *Biomedical engineering letters*, vol. 7, pp. 325-332, 2017.

[52] Y. Hu, Y. Zhao, J. Liu, J. Pang, C. Zhang and P. Li., "An effective frequency-domain feature of atrial fibrillation based on time-frequency analysis," *BMC Medical Informatics and Decision Making* , vol. 20, pp. 1-11, 2020.

[53] A. A. R.-M. Mjahad, M. Bataller-Mompeán, J. V. Francés-Villora and J. F. Guerrero-Martínez, "Ventricular Fibrillation and Tachycardia detection from surface ECG using time-frequency representation images as input dataset for machine learning," *Computer methods and programs in biomedicine*, vol. 141, pp. 119-127, 2017.

[54] K. Gadzicki, R. Khamsehashari and C. Zetzsche, "Early vs late fusion in multimodal convolutional neural networks.," in *IEEE IEEE 23rd international conference on information fusion (FUSION)*, 2020.

[55] M. K. e. al., "Multimodal deep learning for biomedical data fusion: a review.," *Briefings in Bioinformatics*, vol. 33, no. 2, p. bbab569, 2022.

[56] F. Zhao, C. Zhang and B. Geng, "Deep multimodal data fusion," *Zhao, F., Zhang, C. and Geng, B.*, vol. 56, no. 9, pp. 1-36, 2024.

[57] Q. Yang, Y. Zhao and H. Cheng, "MMLF: Multi-modal Multi-class Late Fusion for Object Detection with Uncertainty Estimation.," *arXiv preprint*, p. arXiv:2410.08739, 2024.

[58] Y. Pandeya and J. Lee, "Deep learning-based late fusion of multimodal information for emotion classification of music video," *Multimedia Tools and Applications*, vol. 80, no. 2, pp. 2887-2905, 2021.

[59] T. Oladunni, "Rethinking Multimodality: Optimizing Multimodal Deep Learning for Biomedical Signal Classification," *IEEE Access*, Submitted Manuscript 2025.

[60] T. Baltrušaitis, C. Ahuja and L. -P. Morency, "Multimodal Machine Learning: A Survey and Taxonomy," *IEEE Transactions on Pattern Analysis and Machine Intelligence*, vol. 41, no. 2, pp. 423-443, 2019.

[61] S. Y. Boulahia, A. Amamra, M. R. Madi and S. Daikh, "Early, Intermediate, and Late Fusion Strategies for Robust Deep Learning-Based Multimodal Action Recognition," *Machine Vision and Applications*, 2021.

[62] S. Y. Boulahia, A. Amamra, M. R. Madi and S. Daikh, "Early, intermediate and late fusion strategies for robust deep learning-based multimodal action recognition," *Machine Vision and Applications*, vol. 32,

no. 6, article 121, , vol. 32, no. 6, p. 121, 2021..

[63] M. Hussain, M. O’Nils, J. Lundgren and S. J. Mousavirad, "A Comprehensive Review on Deep," *IEEE Access*, pp. 180093-180124, 2024.

[64] C.-P. F. M. JC, C.-S. D, G. O, R. I and H. LJ., "Machine-Learning-Based Late Fusion on Multi-Omics and Multi-Scale Data for Non-Small-Cell Lung Cancer Diagnosis.,," *J Pers Med*, vol. 14, no. 601, p. 12, 2022.

[65] L. W. H. Wang and W. Li, "A survey on deep multimodal learning for computer vision: Advances, trends, and challenges.,," *Information Fusion*, vol. 77, pp. 149-171, 2022.

[66] Y. Zhang, J. Z. C. Wang and Z. Han, ", "Adaptive fusion of deep neural networks for multimodal emotion recognition,,," *IEEE Transactions on Multimedia*, vol. 23, p. 3145–3158, 2021.

[67] M. S. K. et al., "Multimodal deep learning for biomedical data fusion: a review," *Briefings in Bioinformatics*, vol. 23, 2022.

[68] P. Kumar and V. K. Sharma, " Detection and Classification of ECG Noises using Decomposition Techniques and Machine Learning. .," *Healthcare Technology Letters*, 2020.

[69] M. Živanović, T. Koš and Ž. Čojašić, " Simultaneous Powerline Interference and Baseline Wander Removal in ECG Signals Using a Sinusoidal Model.,," *Przeglad Elektrotechniczny*, vol. 89, no. 5, pp. 121-124, 2013.

[70] K. M. K. B. W. P. C. K. T. Strzecha, G. Lisowski, V. Mosorov and D. Sankowski., " Processing of EMG Signals with High Impact of Power Line and Cardiac Interferences," *Applied Sciences* 11, vol. 11, 2021.

[71] M. S. K. e. al., "Multimodal deep learning for biomedical data fusion: a review," *Briefings in Bioinformatics*, vol. 23, no. 2, 2022.

[72] S. Y. Boulahia, A. Amamra, M. R. Madi and S. Daikh, ", "Early, intermediate and late fusion strategies for robust deep learning-based multimodal action recognition,,," *Machine Vision and Applications*, vol. 32, p. 121, 2021.

[73] J. Cohen, *Statistical Power Analysis for the Behavioral Sciences*, Hillsdale, NJ: Lawrence Erlbaum Associates, 1988.

[74] T. Chicco and G. Jurman, "The advantages of the Matthews correlation coefficient (MCC) over F1 score and accuracy in binary classification evaluation.,," *BMC Genomics*, vol. 21, no. 1, pp. 6-13, 2020.

[75] S. Strodthoff, A. D. Rieke, D. Wenzel and W. Samek, " "Deep learning for ECG analysis: Benchmarks and insights from PTB-XL," *IEEE Journal of Biomedical and Health Informatics*, vol. 45, p. 1519–1528, 2021.

[76] H. Zhang, M. Y. Liu, C. Finn, S. Levine and A. Hannun, "Interpretability and Trust in Deep Learning for Cardiology," *arXiv preprint*, 2022.

[77] J. Adebayo, J. Gilmer, M. Muelly, I. Goodfellow, M. Hardt and B. Kim, "Sanity checks for saliency maps," in *NeurIPS*, 2018.

[78] S. Tjoa and C. Guan, " "A survey on explainable artificial intelligence (XAI): Toward medical XAI," *IEEE Transactions on Neural Networks and Learning Systems*, vol. 32, no. 11, p. 4793–4813, 2021.

[79] P. Linardatos, V. Papastefanopoulos and S. Kotsiantis, "Explainable AI: A review of machine learning interpretability methods," *Entropy*, vol. 23, no. 1, p. 18, 2021.

[80] P. Schmidt and F. Biessmann, " Quantifying Interpretability and Trust in Machine Learning Systems.,," *arXiv*, p. <https://arxiv.org/abs/1901.08558>, 2019.

[81] T. M. Cover and J. A. Thomas, *Elements of Information Theory*,, Hoboken, NJ, USA: Wiley-Interscience,, 2006.

[82] A. Sharma, D. F. Miranda, H. Rodin, B. A. Bart, S. W. Smith and G. R. Shroff, "Interobserver variability among experienced electrocardiogram readers to diagnose acute thrombotic coronary occlusion in patients with out of hospital cardiac arrest: Impact of metabolic milieu and angiographic culprit," *Resuscitation*, vol. 172, pp. 24-31, 2022.

[83] B. Oliveira, A. Lobo, C. Costa, R. Fontes-Carvalho, M. Coimbra and F. Renna, "Explainable Multimodal Deep Learning for Heart Sounds and Electrocardiogram Classification," in *Annu Int Conf IEEE Eng Med Biol Soc.*, 2024.

[84] A. H. e. al., "Accurate Atrial Fibrillation Detection Using Deep Learning on ECGs," *Nature Biomedical Engineering*, vol. 3, p. 112–119, 2019..

[85] S. Kiranyaz, T. Ince and M. Gabbouj, "Real-Time Patient-Specific ECG Classification by 1-D Convolutional Neural Networks," *IEEE Trans. Biomed. Eng.*, vol. 63, no. 3, p. 664–675, 2020.

[86] M. Goettling, A. Hammer and H. e. a. Malberg, "xEKGArch: a trustworthy deep learning architecture for interpretable ECG analysis considering short-term and long-term features," *Sci Rep*, p. 13122, 2024.

[87] S. Song and S. Lee, "Comparative study of time-frequency transformation methods for ECG signal classification," *Frontiers in Signal Processing*, vol. 4, pp. 1-10, 2024.

[88] W. Wang, J. Li, Y. Zhang and A. Shashikumar, "Saliency maps provide insights into artificial intelligence-based electrocardiography models for detecting hypertrophic cardiomyopathy," *European Heart Journal – Digital Health*, vol. 4, no. 4, p. 463–474, 2023.

[89] S. Hangaragi and N. J. K. e. a. Neelima, "Integrated fusion approach for multi-class heart disease classification through ECG and PCG signals with deep hybrid neural networks," *Sci Rep*, vol. 15, p. 8129, 2025.

[90] Z. R. Khavas and Babak Mohammadzadeh Asl, "Robust heartbeat detection using multimodal recordings and ECG quality assessment with signal amplitudes dispersion," *Computer Methods and Programs in Biomedicine*, vol. 163, pp. 169-182, 2018.

[91] B. Chen, W. Guo, B. Li, R. K. Teng, M. Dai, J. Luo and H. Wang, "A study of deep feature fusion based methods for classifying multi-lead ECG," *arXiv*, p. 188.

[92] T. GA, J. H. W. K. L. Y. L. J. C. J and Z. T., "DeepMI: Deep multi-lead ECG fusion for identifying myocardial infarction and its occurrence," *Artif Intell Med.* 2021, p. 102192, 2021.

[93] W. H. Organization., "Cardiovascular diseases (CVDs).," [Online]. Available: <https://www.who.int/health-topics/cardiovascular-diseases>. [Accessed 02 07 2025].

[94] C. f. D. C. a. Prevention, "FastStats - Heart Disease," [Online]. Available: <https://www.cdc.gov/nchs/faststats/heart-disease.htm>. [Accessed 02 07 2025].

[95] J. Vergara and P. Estévez, "A review of feature selection methods based on mutual information," *Neural Comput & Applic*, vol. 24, p. 175–186, 2014.

[96] T. 2. 1. 6. Kvålseth, "On Normalized Mutual Information: Measure Derivations and Properties," *Entropy*, vol. 19, no. 11, p. 631, 2017.

[97] Pranav Rajpurkar, A. Y. Hannun, M. Haghpanahi, C. Bourn and A. Y. Ng, "Cardiologist-Level Arrhythmia Detection with Convolutional Neural Networks," *Nature Medicine*, p. 413–420, 2017.

[98] A. C. e. al, "Multimodal ECG Analysis Using Late Fusion of CNNs for Arrhythmia Detection," *Biomedical Signal Processing and Control*, vol. 68, p. 102–117, 2021.

[99] H. Z. e. al, "Fusion of 1D-CNN and Transformer for ECG Classification," *Computers in Biology and Medicine*, vol. 143, p. 105207, 2022.

[100] M. A. A. Rahhal, M. Bazi, H. Alhichri, F. M. N. Alajlan and R. Yager, "Deep learning approach for active classification of electrocardiogram signals," *Information Sciences*, vol. 345, p. 340–354, 2016.

[101] e. a. S. A. Rajpurkar, " Cardiologist-level arrhythmia detection with convolutional neural networks,," *Nature Medicine*, vol. 25, no. 1, pp. 66-69, 2019.

[102] A. Samanta, M. Karlov, M. Ravikumar, C. M. Clarke, J. Rajadas and K. Hassani, "MVMTnet: A Multi-variate Multi-modal Transformer for Multi-class Classification of Cardiac Irregularities Using ECG Waveforms and Clinical Notes," *arXiv preprint*, 2023.

[103] A. Apostol and u. Maria Nut, "Arrhythmia Classification from 12-Lead ECG Signals," *arxiv*, 2025.

[104] Z. Wang, "Probing an AI regression model for hand bone age determination using gradient-based saliency mapping,," *Scientific reports*, vol. 11, no. 1, p. 10610, 2021.

Timothy Oladunni received the master's and Ph.D. degrees in computer science from Bowie State University, MD, USA, in 2013 and 2017, respectively. He is currently an Assistant Professor of Computer Science at Morgan State University, MD, USA. He was a Visiting Assistant Professor of Computer Science at Yale University, CT, USA.

Timothy is a distinguished computer scientist, professor, and machine learning researcher specializing in biomedical signal processing, natural language processing, deep learning, and multimodal AI architecture. With a background in electrical engineering, he has dedicated his research to advancing ECG signal analysis, natural language processing, and pattern recognition.

His recent work has focused on multimodal deep-learning architecture, particularly the trade-off between model complexity and performance in biomedical signal classification. By integrating the time, frequency, and time-frequency domain features, he explores novel ways to optimize CNN-transformer-based models for ECG analysis, ensuring robust and generalizable AI-driven diagnostic systems. As a professor, Timothy is passionate about mentoring the next generation of data scientists and AI researchers.

Ehimen Aneni received his MD and MPH from the University of Ibadan, Nigeria (2004), and Boston University, in Epidemiology & Global Health (2012), respectively. He is currently an Assistant Professor of Medicine (Cardiovascular Medicine) at Yale University, New Haven, CT., USA.



Ehimen's overarching interests are in the promotion of cardiometabolic health in diverse populations through understanding the relationships between cardiovascular diseases (CVDs) and metabolic risk factors. His research is focused on the intersection between obstructive sleep apnea (OSA) and CVD with a sub-focus on elucidating mechanisms of CVDs in OSA. He has recently uncovered a strong association between abnormal myocardial flow reserve (a reduction in the capacity of the heart to increase its blood flow in proportion to its demands) and severe OSA. Abnormal myocardial flow reserve may be a marker of disease of the small blood vessels of the heart (coronary microvascular dysfunction).

Ehimen's work has been presented at national conferences such as the Scientific Sessions of the American College of Cardiology and the American Heart Association. The findings of his research are published in major peer-reviewed scientific journals such as *JACC*, *JACC Cardiovascular Imaging*, *Circulation: Cardiovascular Quality and Outcomes*, *JAHA*, and *Mayo Clinic Proceedings*.

